Database of optical and structural data for the validation of radiative transfer models

Technical Report
Version 04.2015

Andres Kuusk[1], Mait Lang[1,2], Joel Kuusk[1],
Tõnu Lükk[1], Tiit Nilson[1], Matti Mõttus[1,3], Miina Rautiainen[1,3], and Alo Eenmäe[2]

[1] Tartu Observatory, 61602 Tõravere, Estonia
[2] Estonian University of Life Sciences, Institute of Forestry and Rural Engineering, Kreutzwaldi 5, 51014, Tartu, Estonia
[3] University of Helsinki, Department of Forest Resource Management, PO BOX 27, FI-00014, Helsinki, Finland

Tartu Observatory 2015

Contents

Chapter 1

Introduction

Recent advances in airborne and spaceborne scanner technologies have been providing vast amounts of multispectral and multiangular remote sensing data of different spatial and radiometric resolution over the Earth's vegetation. Remote sensing of forests has been one of the major interest in the remote sensing of environment, because forests impact climate, provide different kind of resources for the economy, are related to many species and, on the other hand, are threatened by several anthropogenic factors. There is no realistic alternative to the remote sensing for collecting data frequently and over the large forest areas. However, the analysis and extraction of the information about the forest structure from the forest reflectance recorded on a satellite image, is not a trivial task. Several statistical methods like k-nearest neighbour classification (McRoberts and Tomppo, 2007) are elaborated for creating forest maps from the multispectral satellite images. Mapping of the abrupt changes like clear cuttings from the satellite images can be considered as practical tool for controlling state-wide databases (Lang et al., 2006), but small changes like light thinning cuttings or damages or change in foliage mass and its properties are often difficult to detect.

The formulation of the spectral reflectance of a forest stand can be investigated by using physically based radiative transfer (RT) models for forest canopies. Since several approaches and approximations are used, there have been initiatives to intercompare radiative transfer models in controlled environments. One of these efforts is the RAdiation Model Intercomparison (RAMI) which has reached the beginning of the fourth phase now (Widlowski et al., 2007). In the previous phases of RAMI the models were tested on the simulated data where forest stands and their spectral signatures were generated by combining reflectance models of Monte Carlo type and allometric regression models (Widlowski et al., 2003, 2007). However, to evaluate radiative transfer models in more realistic media, the use of real forest stands together with actual reflectance data should be considered. In addition, the availability of empirical forest structure data accompanied by airborne and spaceborne reflectance measurements will enable the tests of model inversion. Therefore, we present detailed forest structure and reflectance data collected from three real hemiboreal stands in Järvselja, Estonia. This report describes the measurements and compilation the database of the forest structure and optical properties that is intended for forest radiative transfer modeling experiments.

The first note on the database was published in Remote Sensing of Environment in 2009 (Kuusk et al., 2009). Full description of the database is pubilshed in the Vol. 7 of the series of Springer monographs 'Light Scattering Reviews', (Kuusk et al., 2013). New results on the BRF studies are in (Kuusk et al., 2014).

Chapter 2

Study site

There is a forest study area at Järvselja, Estonia which serves as a field base for forestry students of the Estonian University of Life Sciences. The Järvselja Training and Experimental Forestry District is located at 27.268°E and 58.324 °N, Fig. 2.1. A 10×10 km test site for the POLDER mission (Deschamps et al., 1994) was there. Several satellite images (Landsat TM, Spot) of the area have been collected since 1985. The test site serves as a ground truth site for the CHRIS/PROBA mission (Barnsley et al., 2004) as well. Thorough ground measurements on the test site (forest inventory data, LAI, fish-eye images, ground vegetation reflectance spectra) have been performed several times in the frame of the VALERI project (VALERI, 2005).

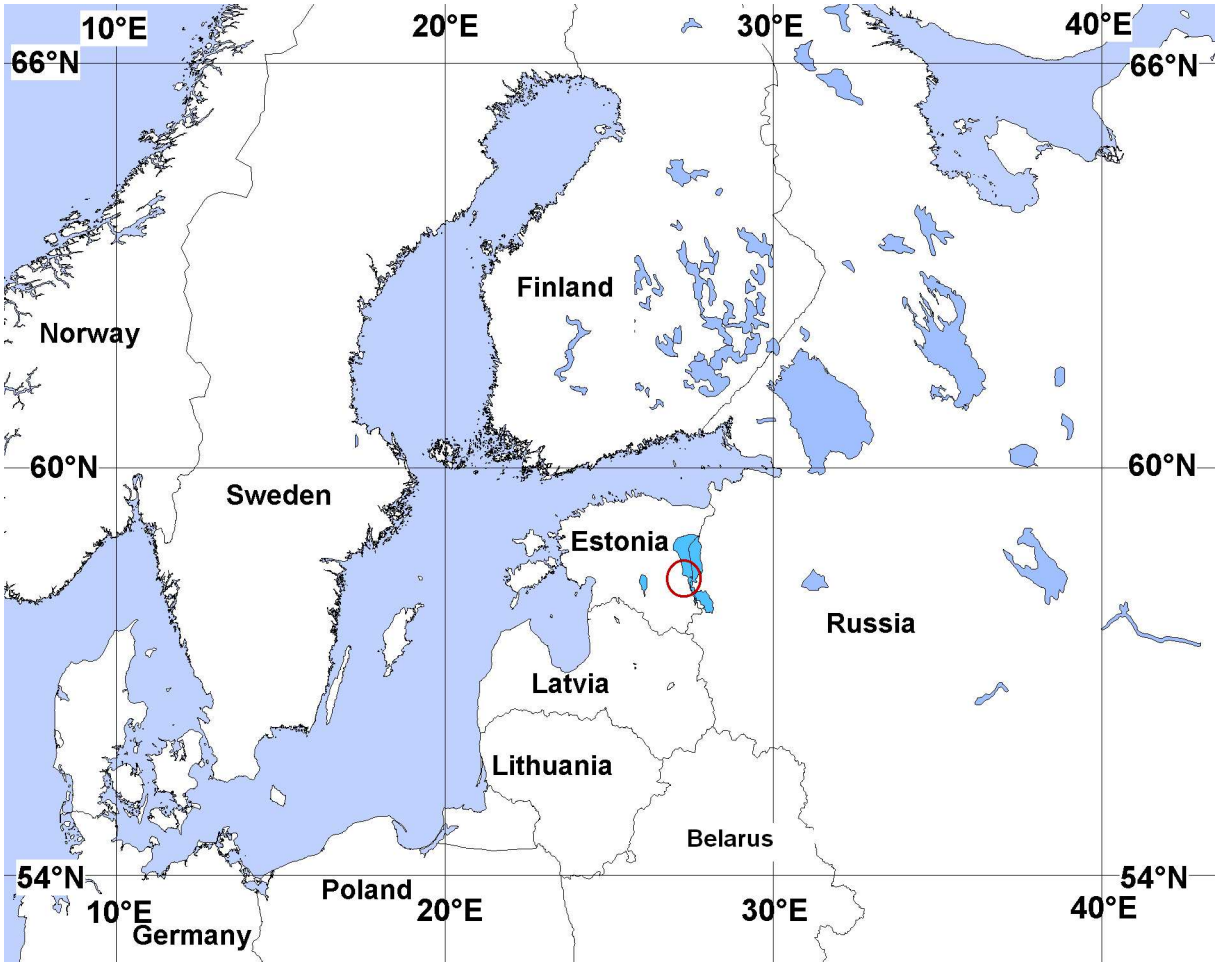

Figure 2.1: Järvselja Training and Experimental Forestry District, Estonia, 27.268°E and 58.324°N. State borders from ESRI (2007).

Järvselja forests are typical for the hemiboreal zone - dominant tree species are Scots pine (*Pinus sylvestris*), Norway spruce (*Picea abies*), Silver and White birch (*Betula pendula, Betula pubescens*), aspen (*Populus tremula*),

Common and White alder (*Alnus glutinosa, Alnus incana*). All these species can grow in pure or mixed stands. Growth conditions range from poor where H_{100} (stand height at the stand age of 100 years) is less than 10 meters to very good where H_{100} can be over 35 meters. All forests are covered by the regular forest inventory from the year 2001. More information on the Järvselja Training and Experimental Forest District can be found on the Internet (Järvselja, 2007).

Three 100×100 m sample plots were selected for the detailed study in summer 2007:
1) a 124 year old *Pinus sylvestris* stand,
2) a 59 year old *Picea abies* stand, and
3) a 49 year old *Betula pendula* stand.

Optical measurements at the test site were carried out in July 2006, August 2007 and July 2008, and a successful CHRIS/PROBA acquisition over the test site was on 10 July 2005.

Chapter 3

Instrumentation

3.1 PROBA/CHRIS imaging spectrometer

CHRIS is a hyperspectral imager on board of the experimental satellite PROBA (Barnsley et al., 2004). CHRIS is used to measure directional spectral reflectance of land areas, thus providing new biophysical and biochemical data, and information on land surfaces.

CHRIS properties:

- multiple imaging of same target area under different viewing and illumination geometries
- spectral range: 415-1050 nm
- spectral resolution: 5-12 nm
- spatial resolution: 17 m at nadir
- swath width: 13 km

The number and bandwidths of spectral bands depend on the selected mode. The Mode 3 (18 spectral bands for land and aerosol studies) was used for the Järvselja acquisition. Spectral bands are listed in Table 5.4.

3.2 Airborne spectrometer UAVSpec

The airborne spectrometer system UAVSpec is based on the 256-band NIR enhanced miniature spectrometer MMS-1 by Carl Zeiss Jena GmbH with the front-end-electronics (FEE) by Tec-5 AG Sensorik und Systemtechnik. It has a wavelength range of 306-1140 nm, 15-bit digital output, and noise level of 2-3 bits. The spectrometer is controlled by an Atmel microcontroller ATmega88. The fore-optics restricts the field-of-view to 2° in airborne measurements. The spectrometer system comprises web camera and a GPS receiver for position tracking. Data from the spectrometer are collected by a PC/104-Plus single board computer Puma by VersaLogic Corp. The spectrometer was also used for the measurements of ground vegetation reflectance with the field-of-view of 8°, for the measurements of incident spectral fluxes during ground vegetation measurements using the ASD's remote cosine receptor (RCR), and for the measurements of leaf and needle reflectance and leaf transmittance with a AvaSphere 50-REFL integrating sphere by Avantes BV.

3.3 Spectrometer FieldSpec-Pro VNIR

The FieldSpec-Pro VNIR spectrometer is a portable 512-channel photo-diode array spectroradiometer by Analytical Spectral Devices, Inc with fiber optic input covering the 350-1050 nm region. The sampling interval is 1.4 nm and the resolution is 3 nm at full width half maximum (FWHM) at 700 nm. The spectrometer was used during CHRIS acquisition and airborne measurements for the irradiance measurements using remote cosine receptor, and for the measurements of leaf reflectance and transmittance using the AvaSphere 50-REFL integrating sphere.

3.4 Spectrometer GER-2600

The GER Corporation 2600 Spectroradiometer for 350-2500 nm spectral range uses a fixed-grating array-based design with two linear arrays - 512 Si detectors and 128 PbS detectors. Spectral bandwidth is 1.5 nm in the spectral range 350 nm to 1050 nm, and 11.5 nm in the spectral range 1050 to 2500 nm, field-of-view 3°. The spectrometer was used for the stem bark reflectance measurements in July 2001.

3.5 LAI-2000 plant canopy analyzer (Li-Cor)

The LAI-2000 plant canopy analyzer uses a fisheye light sensor that measures diffuse radiation in five distinct angular bands about the zenith point. The sensor of the LAI-2000 plant canopy analyzer consists of five concentric photodiodes. The hemispheric image is projected onto these rings, allowing each to measure the radiation in a band at a known zenith angle. The transmitted radiation is restricted below 490 nm, minimizing the contribution of light that has been scattered by foliage. Gap fractions at five zenith angles can be measured by making a reference reading above the canopy (in a forest clearing), and other readings beneath the canopy.

3.6 Coolpix-4500 digital camera

The Coolpix-4500 digital camera was equipped with the Nikon fisheye converter FC-E8, image size 2272x1704 TIFF-RGB. The fisheye converter has 183° FOV and equidistant projection.

3.7 Nikon total station DTM-332

Tree coordinates were measured with Nikon DTM-332 Total station (Nikon-Trimble Co., Ltd., Tokyo, Japan). This device is designed for landsurvey and is equipped with laser distance meter, and records horizontal and vertical angles. Reflector prism was used for measuring distances to the trees with laser distance meter. The total station has one axis tilt sensor and leveling compensation.

3.8 Leica ALS50-II Airborne Laser Scanner

Airborne laser scanning of stands was carried out with Leica ALS50-II Airborne Laser Scanner onboard the special mission aircraft Cessna 208B Grand Caravan by Estonian Land Board on 30 July 2009.

Laser scanner ALS50-II (Leica Geosystems AG, St. Gallen, Switzerland) is a compact laser-based system designed for the acquisition of topographic and return signal intensity data from a variety of airborne platforms. The data is computed using range and return signal intensity measurements recorded in flight along with position and attitude data derived from airborne GPS and inertial subsystems. The lidar collects heights of four return signals. System FOV is adjustable over the range of 0-75 degrees, in 1-degree increments. The scan rate is user-selectable from 0 to 90 Hz in 0.1 Hz increments. The system provides a sinusoidal scan pattern in a plane nominally orthogonal to the longitudinal axis of the scanner, nominally centered about nadir. Output beam divergence is 0.22 mr nominal, measured at the $1/e^2$ point.

Chapter 4

Measurements

4.1 Stand structure

4.1.1 Ground measurements

Detailed structure measurements of the three selected stands were carried out in summer 2007. A square plot of 100×100 m was marked in every stand, and exact positions of all trees with the trunk diameter at breast height $d_{1.3}$ larger than 4 cm were tallied and their locations were mapped using Nikon DTM-332 Total Station. The obtained tree location coordinates are in the radius of 5-20 cm of their true position. Trees were callipered using the electronic caliper Masser Racal (Savcor Group Ltd., OY, FIN-50100 Mikkeli, Finland), and the average of two perpendicular trunk diameter measurements was used as the $d_{1.3}$ estimate. For each tree its social status within the stand was assessed according to its properties and relative size to its neighbours and forest stand average characteristics. Four status classes were distinguished 1) upper layer, 2) second layer, 3) regeneration, and 4) understorey. In order to create allometric models of the tree height and crown dimensions a series of sample trees were measured. Distribution of $d_{1.3}$ and final expert guess were used to distribute sample trees between 1 cm wide $d_{1.3}$ classes according to the total tree count in a particular diameter class. Expert guess was used to add sample trees into the $d_{1.3}$ classes of large or small trees to assure representativeness of the sample for all species and social status classes. Total number of sample trees measured was 73 in the birch stand, 77 in the spruce stand, and 45 in the pine stand. Random sampling from the database was used to identify sample trees. Tree height h, height to live crown base h_{lcb} and two perpendicular crown diameters d_{cr} were measured on each of the sample trees.

Effective leaf area index LAI_{eff} was measured with an LAI-2000 instrument on the regular grid of 9 sample plots L1-L9, the grid step being 30 m, Table 4.1. Measurements were done with two LAI-2000 instruments in overcast weather. Three readings of LAI-2000 was taken at every LAI point L1-L9, and mean gap fractions and LAI were calculated for every Li. In the birch stand effective LAI was measured and hemispherical images were taken twice - with full foliage in July and with no leaves in winter in order to estimate the share that stems and branches have in forming the canopy cover.

Table 4.1: The grid of LAI measurements

ID	Position (x, y), m
L1	(20, 20)
L2	(20, 50)
L3	(20, 80)
L4	(50, 20)
L5	(50, 50)
L6	(50, 80)
L7	(80, 20)
L8	(80, 50)
L9	(80, 80)

Hemispherical color (RGB) images were taken at every LAI point early in the morning with low Sun and no clouds. The blue images were thresholded for estimating gap fractions.

The Cajanus sighting tube was used to obtain canopy closure and crown closure estimate (Jennings et al., 1999) according to the methodology by Korhonen, et al. (2006). Canopy closure is the proportion of canopy overlying the forest floor and crown closure is the ratio of total area of crown projections to the plot area. Crown closure and canopy closure of upper and lower tree layers was measured taking 345-366 readings in a stand. Tree crown envelopes in each stand were visually judged.

4.1.2 Airborne measurements

Airborne laser scanning of stands was carried out with Leica ALS50-II Airborne Laser Scanner onboard the special mission aircraft Cessna 208B Grand Caravan by Estonian Land Board on 30 July 2009. Flying height was 500 m above ground level, point spacing across track 0.24 m, point spacing along track 0.73 m, average point area 0.05 m^2, nadir point density 11 pts/m^2. Every stand was measured twice flying parallel to stand borders over the stand center at perpendicular azimuths, thus the total point density is about 20 pts/m^2.

4.2 Spectroscopic measurements

4.2.1 Reflectance spectra of phytoelements

Directional-hemispherical reflectance and transmittance of birch, alder and aspen leaves in the birch stand, and reflectance of spruce and pine needles was measured using the UAVSpec spectrometer equipped with the integrating sphere AvaSphere 50-REFL by Avantes BV. The AvaLight-HAL tungsten halogen light source by Avantes BV was used. The measurements setup UAVSPEC and AvaSphere_50_REFL together with AvaLight_Hal was calibrated using measurements of Spectralon references SRT-99-100, SRT-20-120, and Zenith Ultrawhite Reflectance Standard 10 cm x 20%, light trap, and white reference tile WS-2 by Avantes BV.

Birch, alder and aspen branches from the upper part of tree crowns were shot down and brought to the spectrometer in less than half an hour. Reflectances of both adaxial and abaxial surface of a leaf attached to the branch and having black background were measured. Several leaves were measured, and mean reflectance spectra and variance were calculated. Pine and spruce branches were cut climbing trees. Reflectance of a bundle of needles in a live shoot was measured. Reflectance spectra of stem and branch bark were measured similar to leaf reflectance. Stem bark directional reflectance of some species was measured previously with a GER-2600 spectrometer using natural illumination (Lang et al., 2002).

4.2.2 Reflectance of ground vegetation

Reflectance spectra of ground vegetation were measured with the UAVSpec spectrometer at LAI points L1-L9 in cloudless conditions. At every LAI point radiance spectra of ground vegetation were measured vertically downward from a height of about 1 m using a field restrictor of 8° and walking along a nearly circular transect of 5 m radius around the LAI point. Then the field restrictor was replaced by the cosine receptor looking upward, and the measurement was repeated. Foreoptics were leveled using self-leveling mount. Data from the spectrometer were collected 8 times per second. The reflectance spectrum for a LAI point is the ratio of these two mean values, calibrated to reflectance factor using the spectralon reference panel. The mean values and standard deviations reported are those over nine LAI points. Sun angles during measurements are listed in Table 4.2.

4.2.3 Airborne measurements

Hyperspectral reflectance of stands was measured with the UAVSpec spectrometer system. The spectrometer was mounted rigidly at the chassis of a Robinson R-22 helicopter, looking in the nadir direction during straight flight at a constant speed. Data from the spectrometer were collected approximately 3-5 times per second in 2006, and 8 times per second in 2007 and 2008. Web camera images, position data from the GPS receiver, and FEE temperature were recorded once per second. During helicopter measurements it was equipped with fore-optics which restricted the field-of-view to 2°. Measurements were made in cloudless conditions from the height of 100 m above ground level in July 2006 and from the height of 80 m in 2007 and 2008 measurements. The flight speed was 60 km/h. The measurement conditions are reported in Table 4.3.

Table 4.2: Sun angles durig understorey measurements

Date	Time, GMT	SZA	SAA
Birch stand			
22.07.2007	12:01-12:42	42.4-46.1	217.5-230.1
25.07.2008	10:06-10:44	38.8-39.1	175.8-189.9
Pine stand			
22.07.2007	08:11-08:52	44.3-41.0	135.4-148.8
05.08.2007	08:22-08:53	46.4-44.1	140.5-150.6
25.07.2008	07:25-08:02	49.7-45.9	122.5-132.9
Spruce stand			
21.07.2007	13:50-14:28	53.6-58.4	248.5-257.7
05.08.2007	10:21-12:07	41.3-46.0	181.6-217.9
25.07.2008	08:57-09:31	41.4-39.7	150.8-162.6

SZA - Sun zenith angle, deg.
SAA - sun azimuth angle, deg.

Table 4.3: Airborne measurements of the test site

Date	26 July 2006	8 August 2007	24 July 2008
Time, GMT	9:19–9:31	9:57–10:46	8:05–8:30
Sun zenith angle	40.3°–39.8°	42.3°–42.4°	45.4°–43.2°
Sun azimuth angle	158.4°–162.7°	172.6°–189.4°	133.8°–141.6°
D_{550}/Q_{550}	0.097	0.262	0.097
Observation nadir angle	0°	0°	0°
Platform altitude	100 m	80 m	80 m

D_{550}/Q_{550} - ratio of downward diffuse and total spectral fluxes at 550 nm

4.2.4 CHRIS images

Images were acquired for one near nadir and two backscattering (hot-spot side) viewing geometries. Acquisition details are listed in Table 4.4.

Table 4.4: CHRIS acquisition details, 10 July 2005

Scene number:	5703	5705	5707
Sun zenith angle		36.6°	
Sun azimuth angle		167.2°	
Platform altitude		562 km	
Image size, pixels		748×744	
Number of spectral bands[1]		18	
Time, GMT	9:43:39	9:44:28	9:45:18
Observation zenith angle	7.62°	37.23°	56.71°
Observation azimuth angle[2]	-22.46°	19.79°	23.43°
Ground resolution, m	17×17	21×19	28×19

[1] Wavelengths and bandwidths see in Table 5.4.
[2] Relative to the Sun azimuth.

4.2.5 Illumination conditions

Downward total Q_λ and diffuse D_λ spectral fluxes were measured at the test site with the FieldSpec Pro spectrometer equipped with a cosine receptor. For the measurement of diffuse sky flux a screening disc was used which screened about 9° of sky in Sun direction. At Tartu Observatory, 45 km from the test site an AERONET sun photometer (Holben et al., 1998) is measuring optical properties of the atmosphere - aerosol optical thickness,

water vapor content from direct sun measurements, and sky radiance distribution along the solar principal plane and along the solar almucantar Sun vertical plane for retrieving size distribution and phase function of aerosol.

Chapter 5

Data processing

5.1 Stand structure

The nonlinear least squares regression method (NLS) of the *R* statistical software (R-project, 2007) was used to estimate parameter values for the allometric models of tree height, crown length, and crown radius (Table 5.1). The arguments for the models were $d_{1.3}$, tree height h in some models, and relative diameter d_r of a given tree with respect to its neighbours located within a radius of 4 m. For the *Fraxinus excelsior* and *Acer platenoides* trees in the birch stand the social status code (1-4) was informative for the crown radius model. Inclusion of arguments into models was judged by the probability value p of their parameter using the criterion $p \leq 0.05$. The aim of the models was mainly to get best fit on the sample tree data and not to search for general purpose model formulas. Goodness of fit r^2 for regression models was calculated as

$$r^2 = 1 - \frac{SSE(n-1)}{SSY(n-k)}, \tag{5.1}$$

where $SSE = \sum_{i=1}^{n}(x_i - \hat{x})^2$ is the sum of squared differences between model $\hat{x}$ and observations x_i, $SSY = \sum_{i=1}^{n}(x_i - x)^2$ is the sum of squared deviation of observations from mean x of the observations, n is the number of observations in the sample, and k is the number of estimated parameters. Standard errors of regression models for tree height, crown length and crown radius are 1.6 m, 1.7 m and 0.28 m, respectively.

Foliage mass for all individual trees was estimated using the equations listed in Table 5.2, and foliage area estimates were obtained using specific leaf weights as given in Table 5.3. Finally, the allometric leaf area index LAI_{all} of the stands was calculated.

5.2 Leaf and needle optical properties

The AvaSphere 50-REFL integrating sphere has only one sample port, the sample reflectance is measured by substitution method. The directional-hemispherical reflectance of a sample r_s is calculated from the spectrometer readings in digital counts measuring the sample B_s and reference B_{st} (Wendlandt and Hecht, 1966),

$$r_s = \frac{B_s}{B_{st}} \frac{\eta_{st}}{\eta_s} r_{st}. \tag{5.2}$$

Here, r_{st} is the reflectance of reflectance standard (reference), and η_x is the sphere efficiency,

$$\eta_x = \frac{1}{(1 - \hat{r}_x)} \frac{b}{S}; \;\; x = s, st, \tag{5.3}$$

S is the total area of the sphere, b is the area of the exit port, r_x is the reflecting power of the sphere,

$$\hat{r}_x = \frac{(r\,d + r_x c)}{S}, \tag{5.4}$$

r is the reflectivity of the sphere surface, $d = S - a - b - c$, a is the area of illumination port, c is the area of the sample port.

Table 5.1: Equations for the tree height, crown radius and crown length

Eq. no	Equation	Stand	Species[1]	r^2, %	RSE, m	n
1	$h = 1.3 + 37.83(d_{1.3}/(d_{1.3} - 1))^{-8.229}$	Birch	KS	86.2	1.89	30
2	$h = 1.3 + 37.79(d_{1.3}/(d_{1.3} + 1))^{8.699}$	Birch	HB	94.1	1.15	6
3	$h = 1.3 + 28.91(d_{1.3}/(d_{1.3} + 1))^{12.66}$	Birch	KU	99.2	0.36	3
4	$h = 1.3 + 36.26(d_{1.3}/(d_{1.3} + 4))^{3.051}$	Birch	LM (PJ, JA)	87.9	1.44	14
5	$h = 1.3 + 29.19(d_{1.3}/(d_{1.3} - 4))^{-1.851}$	Birch	PN	74.9	2.39	14
6	$h = 1.3 + 33.79(d_{1.3}/(d_{1.3} + 1))^{9.988}$	Birch	SA, VA	70.4	2.31	6
7	$h = 1.3 + 33.28(d_{1.3}/(d_{1.3} - 1))^{-6.320}$	Spruce	KS	89.5	1.59	14
8	$h = 1.3 + 37.15(d_{1.3}/(d_{1.3} + 1))^{12.656}$	Spruce	KU	93.5	1.95	63
9	$h = 1.3 + 22.31(d_{1.3}/(d_{1.3} + 8))^{1.152}$	Pine	MA	58.4	1.36	45
10	$h_{lcb} = 26.49(d_{1.3}/(d_{1.3} + 4))^{4.054}$	Birch	LM	50.2	2.91	14
11	$l = 0.3782 d_{1.3}$	Birch	HB	94.6	1.10	6
12	$l = 17.93(d_{1.3}/(d_{1.3} + 8))^{2.049}$	Birch	KS	77.7	2.40	29
13	$l = 31.075(d_{1.3}/(d_{1.3} + 4))^{4.909}$	Birch	PN	80.3	2.12	14
14	$l = 0.5221 h$	Birch	SA, VA	63.0	2.58	6
15	$l = 16.16(d_{1.3}/(d_{1.3} - 1))^{11.154}$	Spruce	KS	92.6	1.34	14
16	$l = (0.1241 h d_{1.3}^{1.333})/d_{1.3} + 2.523 d_r$	Spruce	KU	94.1	1.87	63
17	$l = 12.71(d_{1.3}/(d_{1.3} + 8))^{2.982}$	Pine	MA	86.1	0.79	44
18	$d_{cr} = 1.461 + 0.0899 d_{1.3} d_r$	Birch	HB	98.6	0.57	6
19	$d_{cr} = 1.469 + 0.07193 d_{1.3} d_r$	Birch	KS	98.7	0.58	30
20	$d_{cr} = 1.856 + 0.08579 d_{1.3} d_r$	Birch	LM	98.5	0.51	14
21	$d_{cr} = 0.1836 d_{1.3} + d_r^{-1.088}$	Birch	PN	98.4	0.60	14
22	$d_{cr} = 0.1549 d_{1.3} \cdot Status$	Birch	SA, VA	97.4	0.68	6
23	$d_{cr} = 1.418 + 0.004808 d_{1.3}^2$	Spruce	KS	98.9	0.51	14
24	$d_{cr} = 0.2145 d_{1.3} - 0.8531$	Pine	MA	95.6	0.44	45

[1] Species codes are defined in Table 5.3

h - tree height, m; $d_{1.3}$ - breast height diameter, cm; h_{lcb} - crown base height, m; l - crown length, m; d_{cr} - crown diameter, m; d_r - relative diameter at breast height; RSE - residual standard error

Table 5.2: Equations for foliage mass m

Eq. no	Foliage mass	Species	References and notes
1	$m = 3.13 + 0.05947 d_{1.3}^2 - 0.801 d_{1.3}$	HB	(Tamm, 2000), fresh foliage
2	$m = \exp(-2.6024 + 9.8471(d_{1.3}/(d_{1.3} + 7)) + 0.0260 h$ $-1.6717 \ln(d_{1.3}) + 1.0419 \ln(l - 0.0123 Loc)$	MA	(Marklund, 1988), $Loc = 65$
3	$m = 1.0394 \exp(-3.8719 + 2.1141 \ln(D_{lcb}))$	KS	(Hoffmann and Usoltsev, 2002), D_{lcb} is trunk diameter at live crown base
4	$m = 0.001 \cdot 10^{(0.229 + 2.507 \log_{10}(d_{1.3}))}$	PN, JA	(Wang, 2006) equation for *Amur linden*
5	$m = 3 \cdot 10^{-6}(10 d_{1.3})^{2.5470}$	LM	(Johansson, 1999)
6	$m = 1.064 \exp(-1.5732 + 8.4127 d_{1.3}/(d_{1.3} + 12)$ $-1.5628 \ln(h) + 1.4032 \ln(l))$	KU	(Marklund, 1988)
7	$m = 1.052 \cdot 10^{(-1.62 + 1.778 \log_{10}(d_{1.3}))}$	others	(Martin et al., 1998), equation for *Acer rubrum*

In the AvaSphere 50-REFL integrating sphere a fiber and collimating lens at the illumination port are used for illumination. Therefore a small part of light $(1 - q)$ is falling at the borders of the sample port and creates additional illumination, so the signal is

$$B_x = [q\, r_x + (1 - q)\, r]\, P\, \eta_x. \tag{5.5}$$

The proportion q can be estimated measuring reference $r_s = r_{st}$ and black hole $r_s = 0$,

$$q = \frac{(1 - \xi_0)\, r}{(r_{st} - r)\, \xi_0 + r}, \tag{5.6}$$

Table 5.3: Specific leaf weight SLW

Specium	Code	SLW, g/m^2	Reference
Acer platenoides	VA	69.0	(Martin et al., 1998)
Alnus glutinosa	LM	77.4	(Niinemets and Kull, 1994)
Betula pendula	KS	76.0	(Niinemets and Kull, 1994)
Fraxinus excelsior	SA	69.0	(Martin et al., 1998)
Pinus sylvestris	MA	160.0	(Pensa and Sellin, 2002)
Picea abies	KU	247.0	(Sellin, 2000)
Populus tremula	HB	190.5	(Tamm, 2000), fresh leaves
Tilia cordata	PN	25.5	(Niinemets and Kull, 1994)
Ulmus glabra	JA	38.5	(Niinemets and Kull, 1994)

$$\xi_0 = \frac{B_0}{B_{st}} \frac{\eta_{st}}{\eta_0}.$$

Finally,

$$\begin{aligned} r_s &= \frac{A-\kappa}{C}, \\ \kappa &= \frac{(1-q)}{q} r, \\ A &= (1 - r\,d\,/\,S)\nu\,\frac{B_s}{B_{st}}, \\ C &= 1 + \frac{\nu\,c}{S}\frac{B_s}{B_{st}}, \\ \nu &= \frac{r_{st}+\kappa}{1 - r\,d\,/\,S - r_{st}c\,/\,S}. \end{aligned} \tag{5.7}$$

Leaf transmittance t_s is measured using an external light source and comparing the spectrometer signals of sample B_s and open sample port B_0,

$$\begin{aligned} t_s &= \frac{(1-\hat{r}_s)}{1-\hat{r}_0}\frac{B_s}{B_0}, \\ &= \frac{(1 - r\,d\,/\,S - r_s c\,/\,S)}{(1 - r\,d\,/\,S)}\frac{B_s}{B_0}. \end{aligned} \tag{5.8}$$

Here r_s is the sample reflectance – the reflectance of the leaf side facing the integrating sphere.

5.3 Correction of UAVSpec data

The spectrometer system UAVSpec was used for airborne measurements, for the measurements of understorey vegetation reflectance spectra, and of leaf and needle optical properties. Several technical aspects related to the spectrometer module MMS-1 should be noted. First of all, spectral aliasing affects the NIR signal of the spectrometer. The second order blocking filter which is directly coated on the sensor is not perfect. It lets some visible light cause aliasing effect in the NIR spectral domain. Secondly, straylight contributes to the signal at wavelengths where the sensitivity of the sensor is low. To overcome these metrological problems, we corrected the measured signal for the spectral aliasing and straylight in the following way. The spectrometer was illuminated through a double monochromator and, while scanning the monochromator over the spectral region of the spectrometer, instrument function was measured for all the bands of the spectrometer. By deconvolution, the original signal was restored for every measured spectrum (Kostkowski, 1997). The aliasing correction allowed to extend the reliable NIR spectral domain of the Zeiss MMS-1 spectrometer module for more than 100 nm, (see Figure 5.1).

Finally, the dark current drift due to temperature changes was taken into account. Since it was not possible to take dark current readings during airborne measurements, those recorded before the flight were used together with FEE temperature measurements and empirically measured temperature dependence of dark current,

$$d_\lambda(T) = d_\lambda(T_0) + f(T) - f(T_0), \tag{5.9}$$

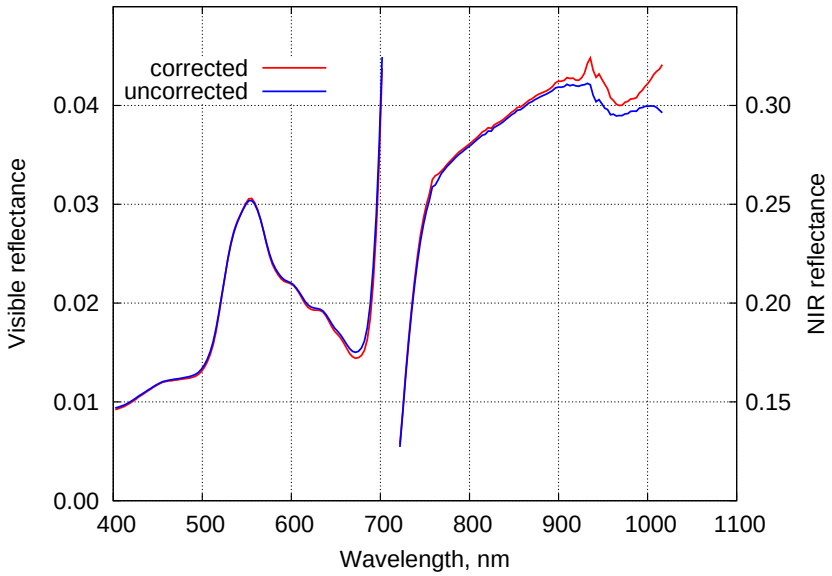

Figure 5.1: Stray light and aliasing correction of a reflectance spectrum.

where $d_\lambda(T)$ is the dark current in case of FEE temperature T, $d_\lambda(T_0)$ is the dark current measured before the flight, T_0 is the FEE temperature during dark current measurement, and f is the temperature dependence of dark current (Schaepman and Dangel, 2000),

$$f(T) = \mathrm{a} + \mathrm{b}\ \exp(\mathrm{c}T), \tag{5.10}$$

where a = 193.06, b = 0.329218, and c = 0.0899416 $^\circ\mathrm{C}^{-1}$ are empirical constants and T is the FEE temperature in Celsius ($^\circ$C). There is no integration time in equations (5.9) and (5.10), therefore, the equations are only valid for an integration time of 120 ms. This integration time was used for measurements of the temperature dependence of dark current, as well as airborne measurements of forest reflectance.

The recorded nadir radiance in digital counts is compared to the radiance of a calibrated Spectralon panel measured in a nearby clearing at the test site just before target measurements. This way the recorded signal is converted to the directional spectral reflectance of targets. To take into account diurnal changes in illumination conditions, downward spectral flux density Q_λ was recorded during measurements with a FieldSpec Pro VNIR spectroradiometer equipped with a cosine receptor,

$$\rho_\lambda(t) = \frac{q_\lambda(t_0)}{n_\lambda(t_0)} \frac{n_\lambda(t)}{q_\lambda(t)} r_\lambda, \tag{5.11}$$

where $\rho_\lambda(t)$ is the target spectral directional reflectance measured at time moment t, $q_\lambda(t)$ and $q_\lambda(t_0)$ are the signals of the FieldSpec spectrometer during target measurements and calibration, respectively, $n_\lambda(t)$ and $n_\lambda(t_0)$ are the signals of the UAVSpec spectrometer, and r_λ is the spectral reflectance of the reference panel. All the signals in equation (5.11) are without dark current. In addition, to calculate the diffuse-to-total flux ratio, a few measurements of downward spectral diffuse flux density D_λ were done, screening direct Sun flux.

5.4 Satellite data

5.4.1 Destriping of images

Destriping of images was performed assuming that striping is caused mainly by sensor offsets. The destriping function was found for every image as the difference between column mean values and smoothed column mean values using 9-point Hamming window (Rabiner and Gold, 1975). The mean value of three destriping functions for every band (scenes 5703, 5705, and 5707) was used for all three respective spectral images.

5.4.2 Atmospheric correction

Satellite-based measurements of the radiative signature of terrestrial targets are always affected by the chemical and physical properties of the overlying atmosphere. Highly accurate, reliable and preferably physically based cor-

rection schemes are thus required to quantitatively link spaceborne measurements with the structural and spectral characteristics of a given vegetation target.

Several procedures have been developed for the atmospheric correction of satellite remote sensing data. A comprehensive overview of atmospheric correction procedures can be found in (Liang, 2004). Thorough comparisons of various procedures of the atmospheric correction of Landsat Thematic Mapper images are reported by Hadjimitsis et al. (2004), and Song and Woodcock (2003). Here, atmospheric correction is performed with atmospheric RT package 6S (Vermote et al., 1997) using the look-up-table method suggested by Kuusk (1998). Atmospheric correction was performed in two stages. First, with the 6S model a look-up-table (LUT) was generated which links top-of-atmosphere (TOA) radiance to top-of-canopy reflectance. The later was calculated with the multispectral homogeneous canopy reflectance model MSRM (Kuusk, 1994) varying ground vegetation parameters. The MSRM model served as the underlying surface in the 6S model, and leaf area index, soil reflectance and leaf optical parameters were varied in a reasonable range characteristic for the test site in order to produce TOA radiance values in the range similar to what we have in CHRIS images. In the calculation of TOA radiance the optical parameters of the atmosphere are needed. An AERONET Sun photometer (Holben et al., 1998) is working at Tartu Observatory, 45 km far from the test site, and the 6S model has tools for using AERONET sun-photometer data directly. Aerosol optical thickness, size distribution and refraction index, and amount of water vapor in the atmosphere were determined from the Sun photometer measurements. Level 2 data were used. Ozone data are available from NASA/GSFC Ozone Processing Team at their web-page (McPeters, 2007). For stable weather conditions, and based on an analysis of MODIS images (MODIS, 2005) and air parcel trajectories of HYSPLIT (2007) for 10 July 2005, it was concluded that significant differences in atmosphere properties over a distance of 45 km were not possible, only small changes in the amount of aerosol and water vapor may be present. On this basis the diffuse spectral fluxes in the atmosphere and the diffuse-to-total ratio of downward spectral fluxes D_λ/Q_λ were calculated with the atmospheric RT model. Simultaneous to the CHRIS acquisition the diffuse-to-total ratio of downward spectral fluxes D_λ/Q_λ was measured at the test site with a FieldSpec Pro spectrometer. In Figure 6.2 we see that the simulated downward diffuse flux using AERONET aerosol optical thickness (at 550 nm τ_{550} = 0.08) exceeds the measured one for some extent. This discrepancy may be caused by differences in the separation of total flux to direct and diffuse fluxes. The field-of-view of the Sun-photometer is 1° while the FieldSpec cosine receptor was screened with a disk which screened about 9° in the Sun direction during sky flux measurements. In the 6S model the direct flux is collimated.

The created LUTs were approximated by a second order polynomial separately for every CHRIS band and every view direction,

$$\rho_{\lambda,j}(b_{\lambda,j}) \;=\; a_{2,\lambda,j}\, b_{\lambda,j}^2 \;+\; a_{1,\lambda,j}\, b_{\lambda,j} \;+\; a_{0,\lambda,j}. \tag{5.12}$$

Here, $b_{\lambda,j}$ is the TOA radiance, and $\rho_{\lambda,j}(b_{\lambda,j})$ is canopy directional reflectance at wavelength λ in the acquisition geometry of CHRIS scenes $j = 5703, 5705, 5707$ (see Table 4.4). The approximation polynomials were used for the calculation of top-of-canopy reflectance using the TOA radiance measured by CHRIS. This procedure was applied separately to every pixel in every spectral image. The advantage of using LUT if compared to the built-in procedure of atmospheric correction in the 6S model is considering the directional dependence of diffuse fluxes scattered from vegetated surface and its variations as a function of wavelength, LAI, and other canopy parameters.

The second step in the atmospheric correction procedure involves the removal of adjacency effects by 2-D deconvolution in CHRIS scenes 5703 and 5705. This is because the atmosphere acts as a low-pass filter which degrades satellite images. The recorded image is a convolution of the top-of-canopy radiance pattern and point spread function (PSF) of the atmosphere (Banham and Katsaggelos, 1997),

$$g(x, y) = p(\xi, \eta) \otimes f(u, v), \tag{5.13}$$

where $f(u, v)$ is the original (ideal) image, $p(\xi, \eta)$ is the PSF of the atmosphere, and $g(x, y)$ is the recorded (degraded) image, $\otimes$ denotes the convolution in the x-y-space.

Degraded images can be restored using Wiener filtering in the Fourier space (Banham and Katsaggelos, 1997; Podilchuk, 1998). The convolution of the original image and PSF in the x-y-space (Eq. (5.13)) can be performed by filtering in the 2D Fourier space

$$G = P \cdot F, \tag{5.14}$$

where G, P and F are the Fourier images of $g(x, y)$, $p(x, y)$ and $f(x, y)$, respectively. The original image is restored by the inverse filtering

$$\hat{F} = G \cdot W, \tag{5.15}$$

where W is the Wiener filter (Podilchuk, 1998)

$$W = \frac{P^* F}{|P|^2 F + S_n}. \tag{5.16}$$

Here the superscript $*$ denotes the complex conjugate, and S_n is the noise spectrum. Inverse Fourier transform of the filtered spectrum $\hat{F}$ returns the corrected image $\hat{f}(x, y)$.

The point spread function (PSF) of the atmosphere as a function of aerosol optical thickness was estimated by Liang et al. (2001) in numerical simulations,

$$p(s) = f_1(\tau)\exp(-q_1 s) + f_2(\tau)\exp(-q_2 s), \tag{5.17}$$

where

$$\begin{aligned} f_1(\tau) &= 0.03\tau \\ f_2(\tau) &= 0.071\tau^3 - 0.061\tau^2 - 0.439\tau + 0.996 \\ q_1 &= 1.424 \ \ \mathrm{km}^{-1} \\ q_2 &= 12916\,\mathrm{km}^{-1}. \end{aligned} \tag{5.18}$$

Here s is the radial distance from the pixel (km) and τ is the optical thickness of the atmospheric aerosol.

The noise spectrum S_n was supposed exponentially increasing with spatial frequency, magnitude of it was estimated using signal/noise ratio from CHRIS documentation (CHRIS, 2002), and the mean reflectance of every spectral image.

Unfortunately, the horizontal range of the adjacency effect seems to be overestimated in (Liang et al., 2001) - the corrected red and NIR reflectance of a narrow lake in the scene turned to negative values. Reflectance of natural water bodies may be well below 1% (Froidefond et al., 2002; Novo et al., 2004; Feng et al., 2005; Cannizzaro and Carder, 2006) but cannot be less than zero. This was the criterion for recalibrating the scale parameters q_1 and q_2 of the PSF by a factor of 4,

$$\begin{aligned} q_1 &= 5.70\,\mathrm{km}^{-1} \\ q_2 &= 5.17 \cdot 10^4\,\mathrm{km}^{-1}. \end{aligned} \tag{5.19}$$

The relative change of the mean stand reflectance due the adjacency correction $(\rho_2(\lambda) - \rho_1(\lambda))/\rho_2(\lambda)$ is plotted in Figure 5.2, where $\rho_1(\lambda)$ and $\rho_2(\lambda)$ are the stand reflectance before and after adjacency correction, respectively.

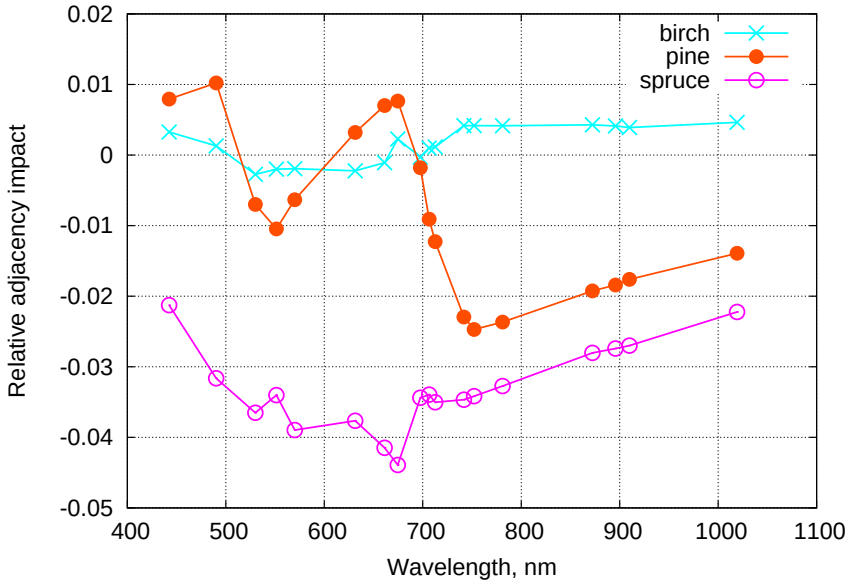

Figure 5.2: The role of adjacency correction.

This procedure of adjacency correction cannot be applied in the case of oblique view (the scene 5707). Then the view path crosses atmosphere layers over different targets, and the prepositions of PSF derivation are not fulfilled. Possible errors in adjacency correction increase with increasing view angle (Reinersman and Carder, 1995).

5.4.3 CHRIS calibration revised

The radiometric calibration of satellite sensors is problematic. Calibration procedures of optical sensors of large satellites have been developed for years and calibration is provided by a mixture of on-ground and in-orbit measurements (Slater et al., 1996; Slater and Biggar, 1996; Thome et al., 1997; Abdou et al., 2002). Preflight calibrations

are subject to change during launch and exposure to the space environment. With increasing time since the launch the role of in-orbit methods increase, however small platforms offer limited scope for on-board calibration facilities. Therefore some vicarious method should be used as an option. For the vicarious calibration of sensors on board large operational satellites which measure continuously large areas (TM, ETM+, HRV, MISR) one can choose bright stable targets at good atmospheric conditions (Abdou et al., 2002). The small acquisition resource of the CHRIS imaging spectrometer on board the PROBA satellite (Barnsley et al., 2004) - two-three sites of about 15×15 km per day - limits also opportunities for the vicarious calibration of the spectrometer. Begiebing and Bach (2004), and Guanter et al. (2005) reported problems in CHRIS NIR calibration comparing CHRIS-derived reflectance spectra to ground measurements. They suggested to revise the CHRIS NIR calibration and that was done by CHRIS team in 2005 (Cutter and Johns, 2005). However, a small satellite is limited in keeping stable conditions of its instruments (Cutter, 2004) and more frequent vicarious calibration of sensors is needed. In the CHRIS scene over the forest test site Järvselja we cannot find bright targets large enough for satellite measurements. Therefore, the CHRIS calibration is validated against top-of-canopy directional reflectance of large forest stands measured on board a helicopter. Our data show that in 2005 revised calibration data are over-corrected.

Reflectance spectra of several homogeneous stands in the CHRIS scene 5703 were compared to airborne measured data of 26 July 2006. Spectral bands of the UAVSpec were combined to the equivalent CHRIS bands. The footprint of the UAVSpec spectrometer's field-of-view from the height 100 m is 9.5 m^2 which is significantly less than the CHRIS pixel, however altogether 1302 recorded UAVSpec spectra over 520 CHRIS pixels over 63 homogeneous stands were involved in the comparison which represent all dominating species at the test site. Difference in view angles was accounted for by numerical simulations of angular dependence of stand reflectance for these targets with the FRT forest reflectance model (Kuusk and Nilson, 2000). The comparison gave us correction factors for the CHRIS calibration coefficients (Tabel 5.4 and Fig. 5.3). Correction factors were calculated as the ratio of the mean stand directional reflectance from helicopter measurements to the mean top of canopy stand reflectance from CHRIS measurements separately for every stand. Correction factors C_λ and their standard deviations in Table 5.4 are the mean value and standard deviation over 63 stands.

Table 5.4: Mode 3 spectral bands (nm) and the corresponding correction factors for CHRIS calibration coefficients

Band	Low	High	Middle	C_λ	STD
Band 1	437.3	447.8	442.4	0.6373	0.0684
Band 2	484.5	496.1	490.2	0.7658	0.0848
Band 3	524.4	535.9	530.0	0.9687	0.1018
Band 4	545.0	557.9	551.3	0.8756	0.0920
Band 5	564.7	575.4	570.0	1.0063	0.1115
Band 6	624.5	638.6	631.4	1.0439	0.1267
Band 7	653.5	669.2	661.2	1.0587	0.1446
Band 8	669.2	680.2	674.6	1.0720	0.1513
Band 9	691.6	703.4	697.5	1.0281	0.1171
Band 10	703.4	709.6	706.5	1.0973	0.1172
Band 11	709.6	715.7	712.6	1.1456	0.1214
Band 12	735.1	748.6	741.8	0.9907	0.1038
Band 13	748.6	755.6	752.1	1.0294	0.1069
Band 14	770.0	792.5	781.1	1.0116	0.1025
Band 15	858.8	886.2	872.3	1.0028	0.0962
Band 16	886.2	905.2	895.7	1.0208	0.0956
Band 17	905.2	914.9	910.0	1.0021	0.0934
Band 18	997.5	1041.3	1019	0.8978	0.0848

C_λ - correction factor
STD - standard deviation of the correction factor

All three sets of spectral images were radiometrically rescaled using these correction factors.

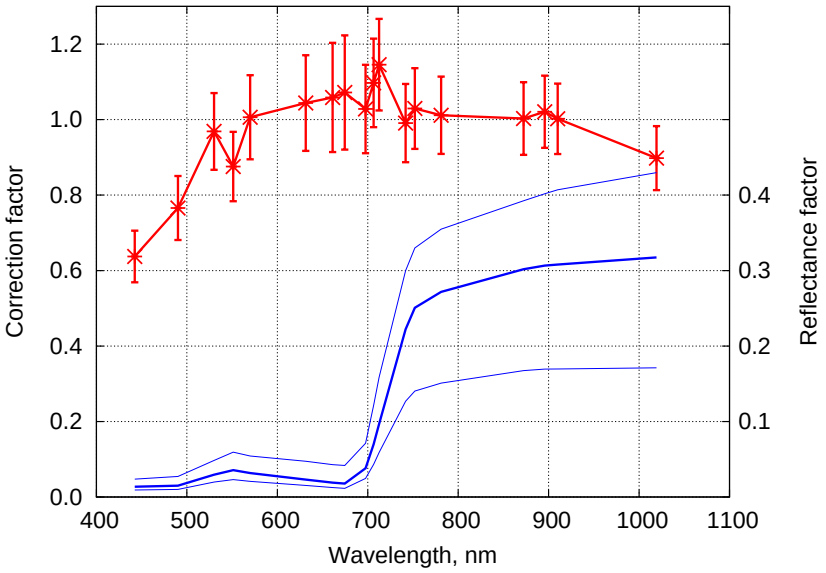

Figure 5.3: Correction factors for CHRIS calibration coefficients (the upper curve with error bars and left axis), and mean stand reflectance and the range of stand reflectances involved in the comparison (the right axis).

Chapter 6

Data

6.1 Illumination conditions

Diffuse-to-total spectral flux ratio D_λ/Q_λ was measured at the test site during PROBA overpass and helicopter measurements. The fish-eye sky image (Fig. 6.1) shows the free horizon at the place of incident flux measurements. During PROBA overpass the aerosol optical depth τ_{550} at AERONET Tõravere station was very low, $\tau_{550} = 0.08$, which is about three times less than in the profiles by Elterman (1968) which are often used in simulation studies. Therefore the D_λ/Q_λ ratio was very low too. During helicopter measurements in 2006 and 2008 the atmosphere transparency was even better than during CHRIS measurements, only in August 2008 the sky flux was during helicopter measurements remarkably higher than during other measurements, Fig. 6.2. Sky spectral radiance in four spectral bands was measured at Tõravere, 45 km from the test site by an AERONET sun photometer. AERONET sun photometer measures sky radiance at almucantar and in the principal plane (Holben et al., 1998). Data are available for dates of satellite and airborne measurements except of 8 August 2007. In Figs 6.3-6.10 are sky radiance profiles for forest observation dates. Data for 9 August 2007 characterise sky radiance during helicopter measurements on 8 August 2007.

Figure 6.1: Fish-eye image at the test site where incident spectral fluxes were measured.

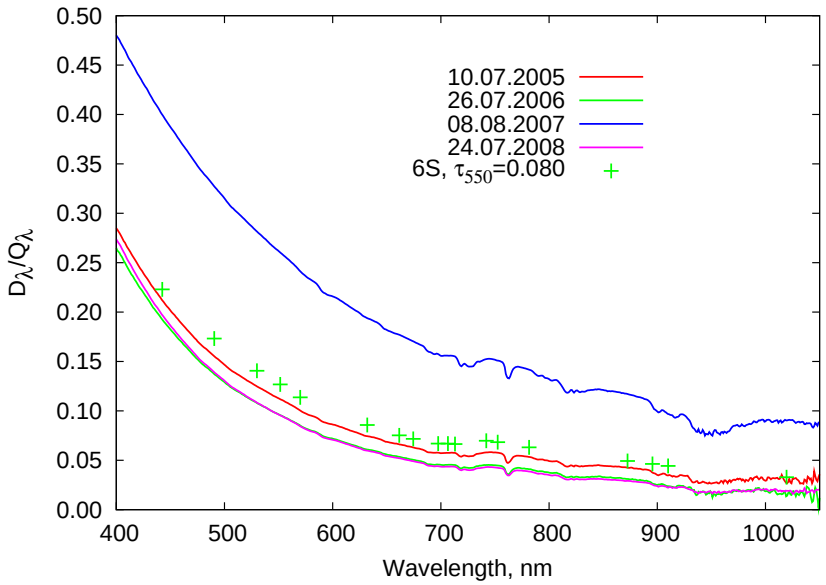

Figure 6.2: Diffuse-to-total flux ratio D_λ/Q_λ from FieldSpec measurements during PROBA overpass (10.07.2005), helicopter measurements (26.07.2006, 08.08.2008, 24.07.2008), and simulated with 6S for CHRIS spectral bands using AERONET level 2 atmosphere data during CHRIS acquisition.

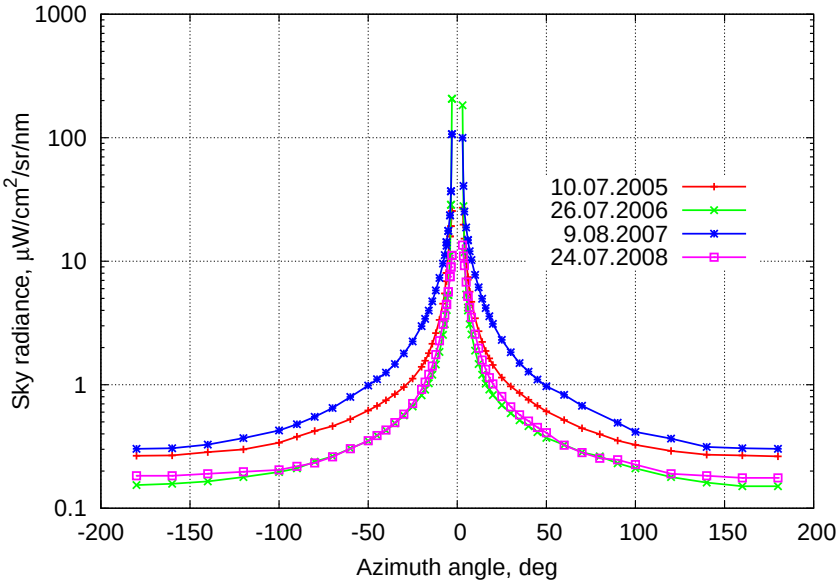

Figure 6.3: Almucantar sky radiance at Tõravere, 1020 nm.

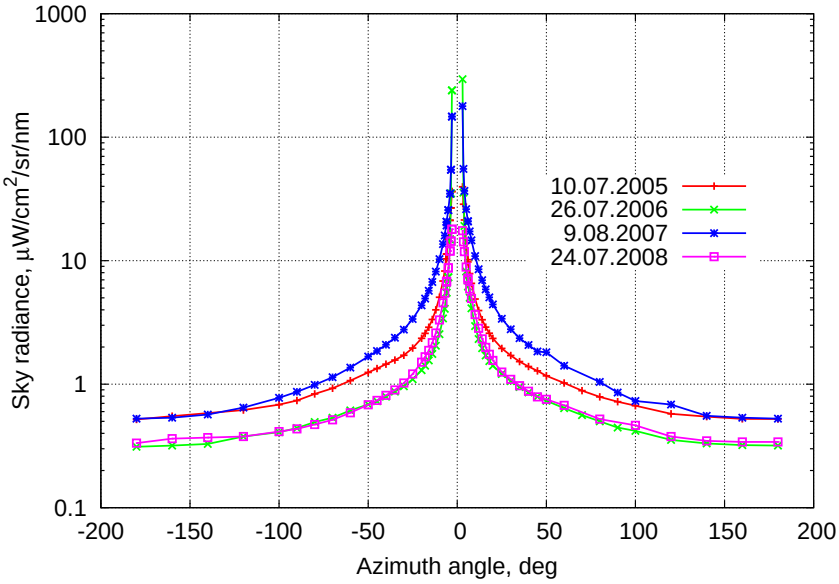

Figure 6.4: Almucantar sky radiance at Tõravere, 870 nm.

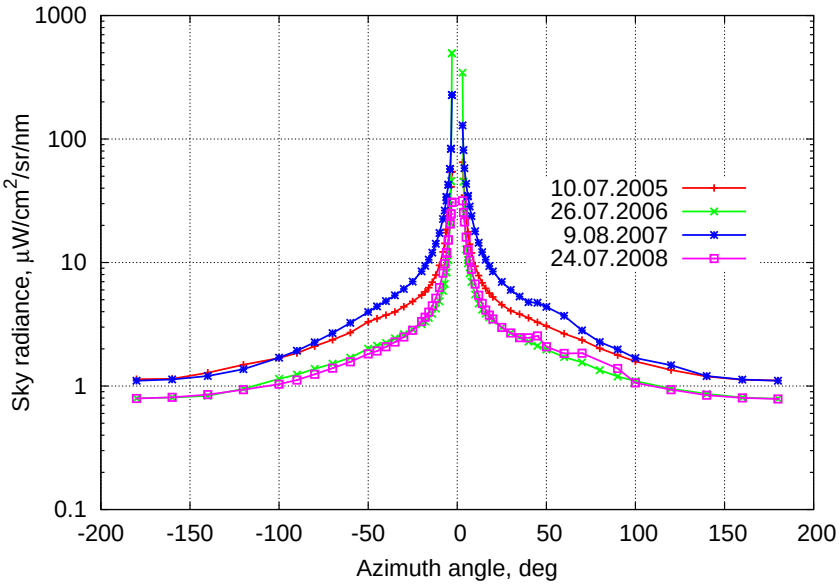

Figure 6.5: Almucantar sky radiance at Tõravere, 675 nm.

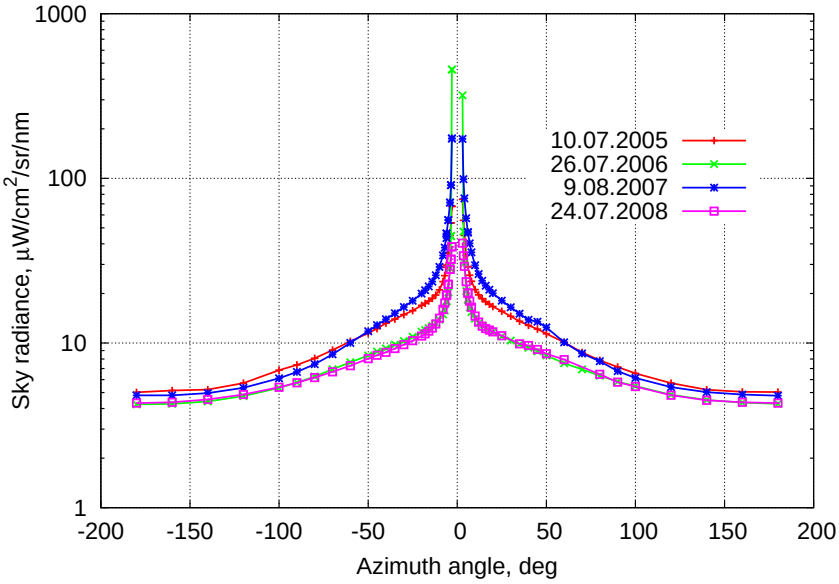

Figure 6.6: Almucantar sky radiance at Tõravere, 440 nm.

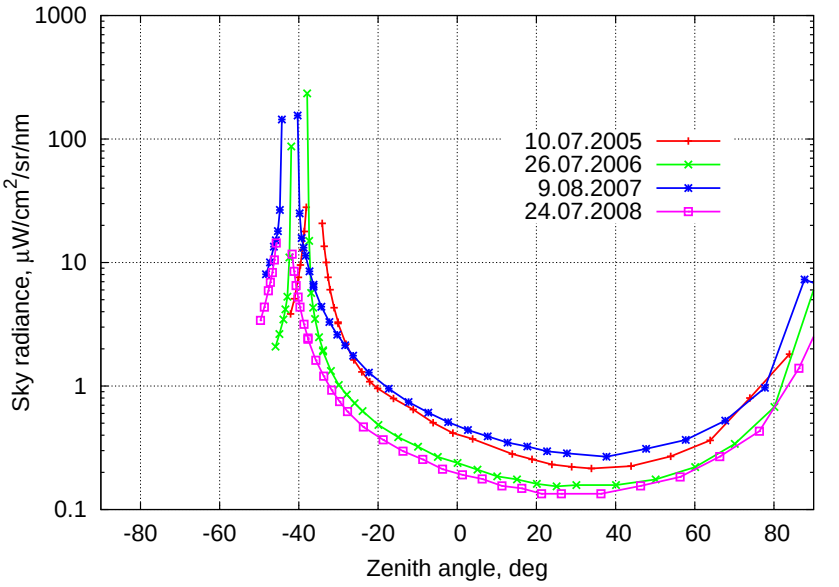

Figure 6.7: Sky radiance in the principal plane at Tõravere, 1020 nm.

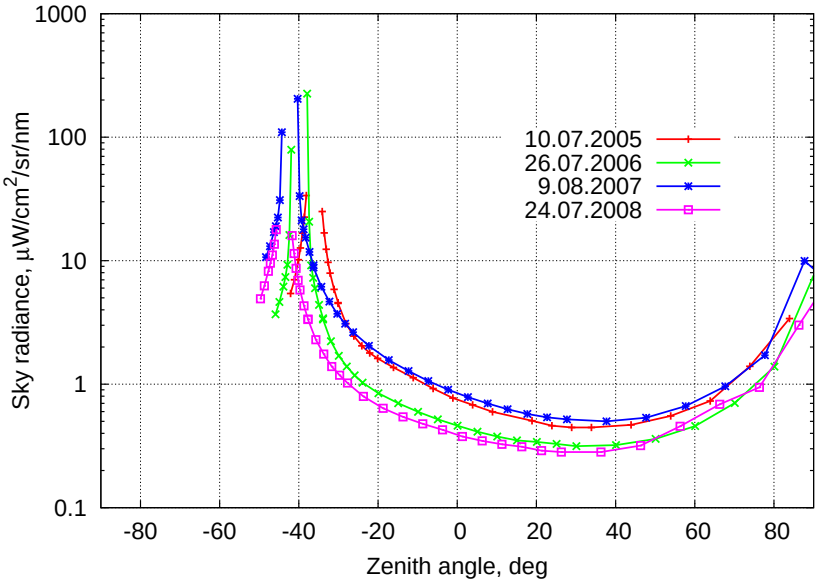

Figure 6.8: Sky radiance in the principal plane at Tõravere, 870 nm.

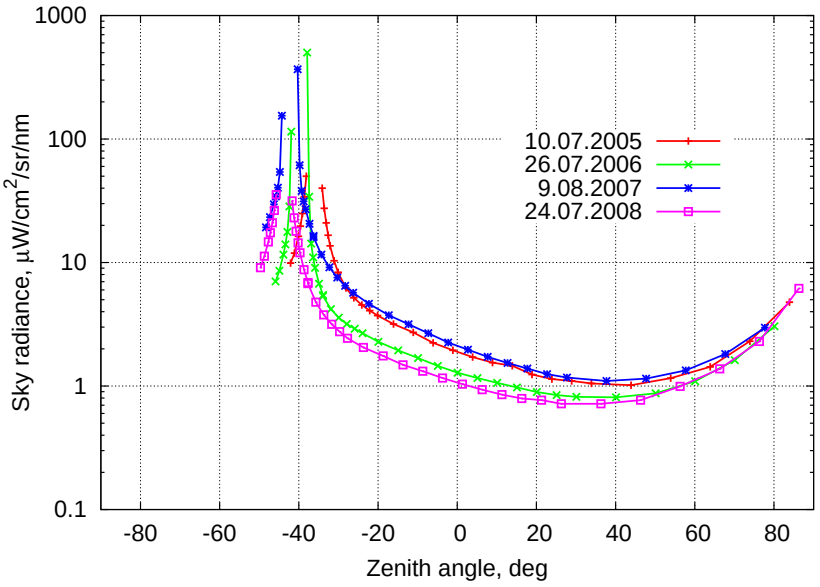

Figure 6.9: Sky radiance in the principal plane at Tõravere, 675 nm.

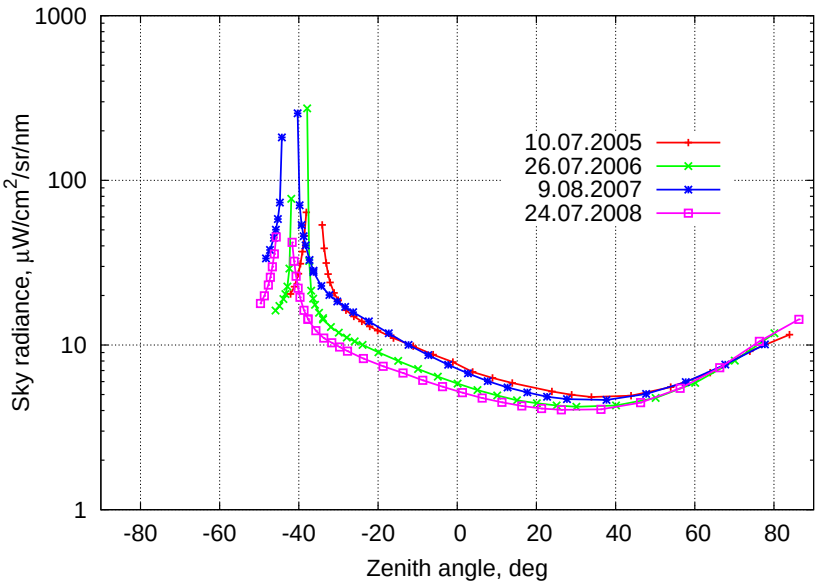

Figure 6.10: Sky radiance in the principal plane at Tõravere, 440 nm.

6.2 Stands

Canopy closure and crown closure estimates, and effective and corrected LAI values for all three stands are reported in Table 6.1. The Nilson and Kuusk (2004) procedure was applied for the correction of LAI-2000 data. Two different correction procedures were applied: - first, using measured canopy cover and recorded LAI-2000 gap fractions,
- second, one iteration was performed which modified crown radius, and consequently canopy cover and gap fractions in LAI-2000 rings.

Table 6.1: Canopy parameters

Stand	LAI_{all}	LAI_{eff}	STD_{LAI}	LAI_1	LAI_2	CaCl	CrCl
Birch[1]	3.93	2.94/0.80	0.346/0.126	3.14	2.89	0.80	1.09
Pine	1.86	1.75	0.149	2.55	2.21	0.74	0.79
Spruce	4.36	3.76	0.617	5.03	4.32	0.90	1.25

[1] LAI_{eff}(July)/LAI_{eff}(November) STD_{LAI} - standard deviation of LAI_{eff}
LAI_{all} - allometric LAI LAI_{eff} - effective LAI, measured with LAI-2000
LAI_1 - corrected LAI, using measured LAI-2000 gap fractions (Nilson and Kuusk, 2004)
LAI_2 - corrected LAI, using an iteration which modified crown radii (Nilson and Kuusk, 2004)
CaCl - canopy closure CrCl - crown closure

Crown envelopes for deciduous species and Scots pine were most similar to ellipsoidal model. For the upper layer Norway spruce trees about 20% of the lower crown was close to cylinder and the upper part was characteristically cone-shaped. Norway spruces in lower tree layers had cone-shaped crowns.

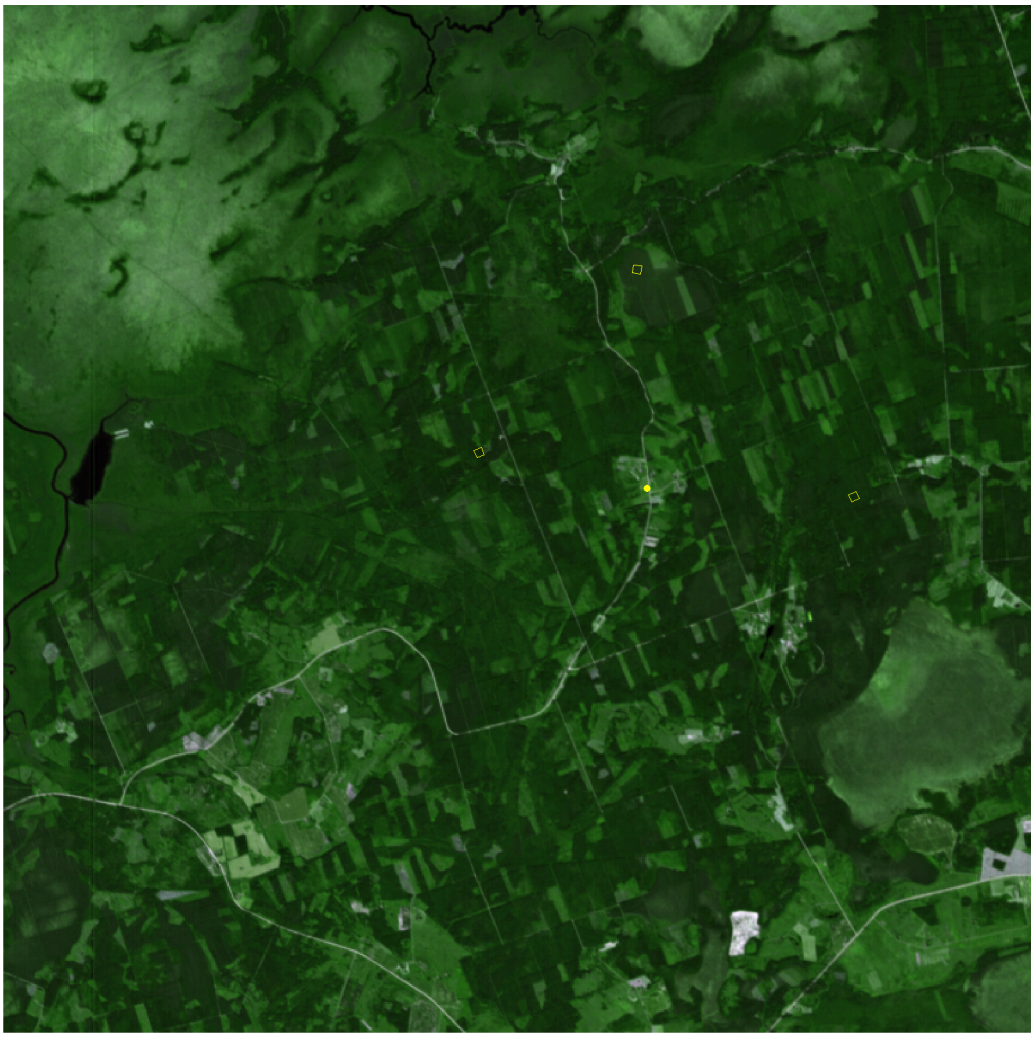

Figure 6.11: The RGB image of the CHRIS scene 5703. Yellow squares mark the selected stands, and the yellow dot marks the place of the FieldSpec measurements of incident radiation. The image size is 12.6×12.6 km.

6.2.1 Birch stand

Structure

This deciduous stand grows on the typical brown gley-soil (*Eutri Mollic Gleysol* – FAO-UNESCO soil classification). Growth conditions are good for forest (H_{100} = 28.7). Stand age is 49 years. Dominating species are birch (*Betula pendula*) 57%, Common alder (*Alnus glutinosa*) 29.5% and aspen (*Populus tremula*) 11%, the total number of trees is 1031. There are two tree layers distinguishable according to the social status of the trees, the lower tree layer is mostly consisting of *Tilia Cordata* and *Picea abies*. Stand was thinned in September-October 2004. Forest understorey vegetation is dominated by the mixture of several grass species. Moss layer is sparse or missing.

Coordinates of the stand center are:
58° 16’ 49.81" N 27° 19’ 51.53" E
L-EST97: X:6464827.8 Y:695338.6.
The origin of local coordinates (x=0, y=0) is
L-EST97: X:6464768.93 Y:695299.41.
Azimuth of the y-coordinate is 348.7°.

The perspective and vertical view of the stand are in Figs 6.13 and 6.14, respectively. Images are created with SVS software (McGaughey, 1997) using individual tree data.

Table 6.2: Mean tree parameters, the birch stand

Species	Code	N	H	$D_{1.3}$	L	R_{cr}
Upper layer						
Betula pendula	KS	399	26.5	20.7	9.2	1.6
Alnus glutinosa	LM	176	23.4	22.4	9.8	2.0
Populus tremula	HB	78	26.8	21.6	8.2	2.0
Salix ssp.	PJ	1	24.0	23.8	9.9	2.0
Second layer						
Tilia cordata	PN	205	15.9	12.8	8.1	1.9
Betula pendula	KS	66	17.9	10.5	5.6	1.0
Fraxinus excelsior	SA	30	15.4	10.9	4.0	1.6
Alnus glutinosa	LM	20	17.5	13.1	8.5	1.4
Acer platenoides	VA	16	15.7	11.3	4.3	1.9
Ulmus glabra	JA	1	15.9	11.4	8.1	1.0
Regeneration layer						
Picea abies	KU	39	8.9	8.9	4.8	1.2

N - number of trees;
H - mean tree height, m;
$D_{1.3}$ - mean breast-height-diameter, cm;
L - mean length of live crown, m;
R_{cr} - mean maximum radius of crown, m.

Figure 6.12: The birch stand, 10 May 2007.

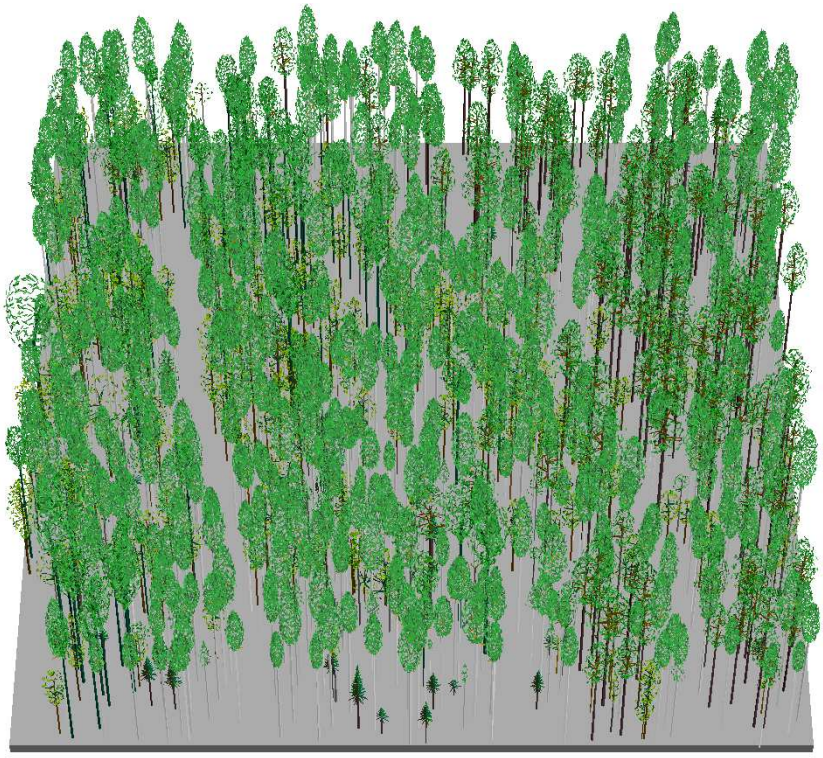

Figure 6.13: The birch stand, perspective view.

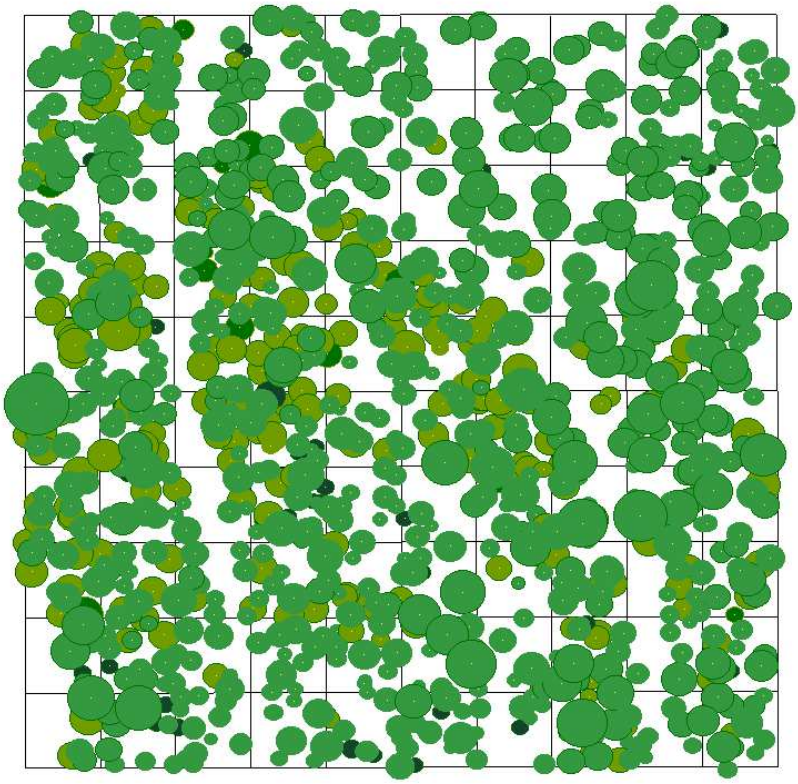

Figure 6.14: The birch stand, vertical view.

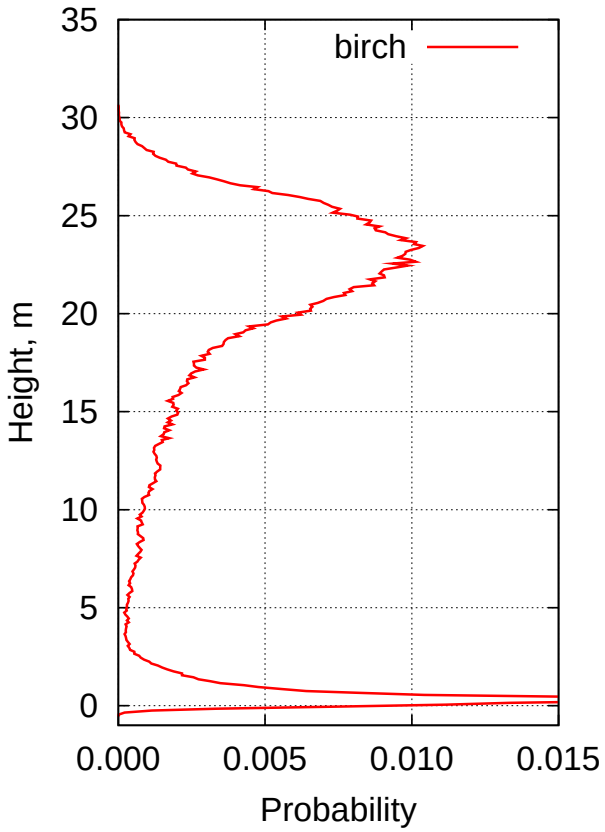

Figure 6.15: Vertical distribution of the lidar first return, the birch stand.

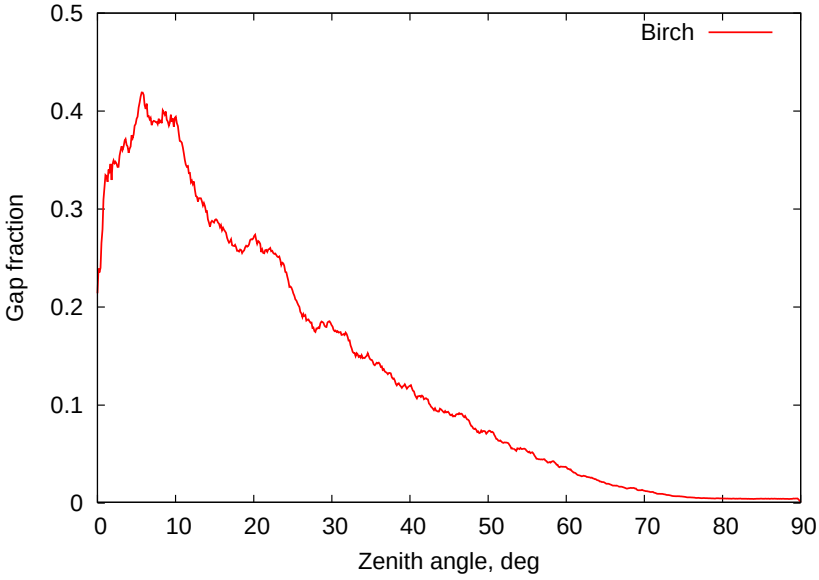

Figure 6.16: Gap fraction in the birch stand, 15.08.2008.

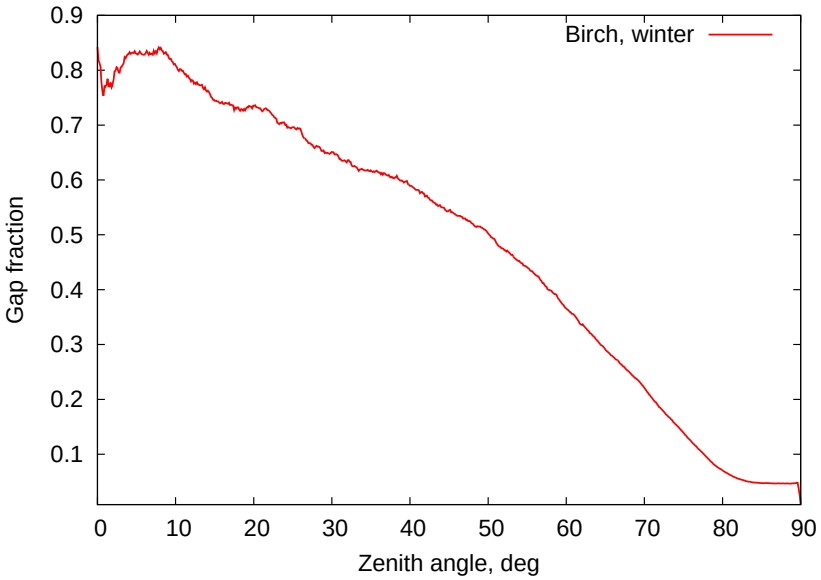

Figure 6.17: Gap fraction in the birch stand, 22.11.2007.

Optical properties

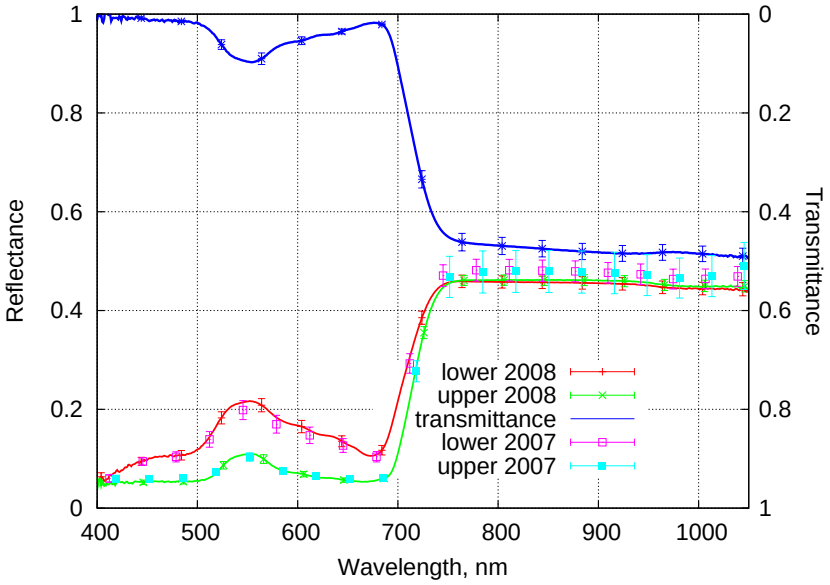

Figure 6.18: Leaf reflectance and transmittance of *Betula pendula*.

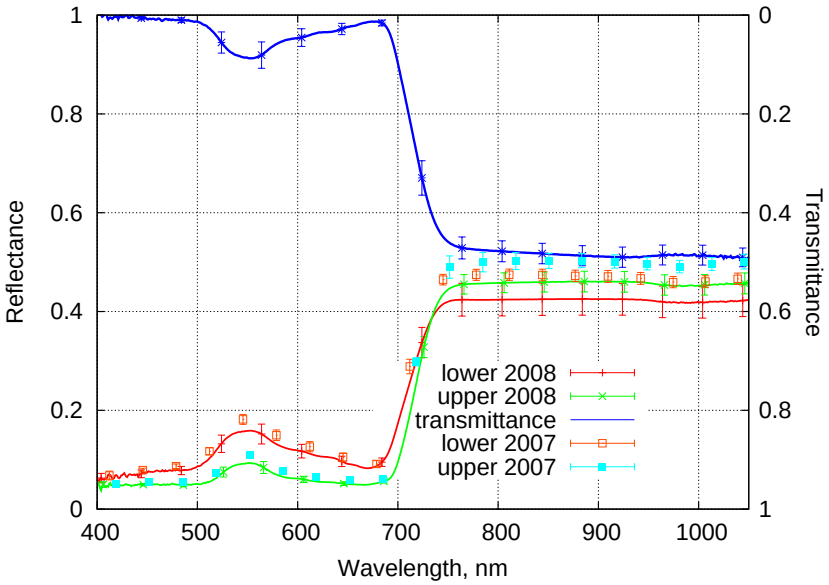

Figure 6.19: Leaf reflectance and transmittance of *Alnus glutinosa*.

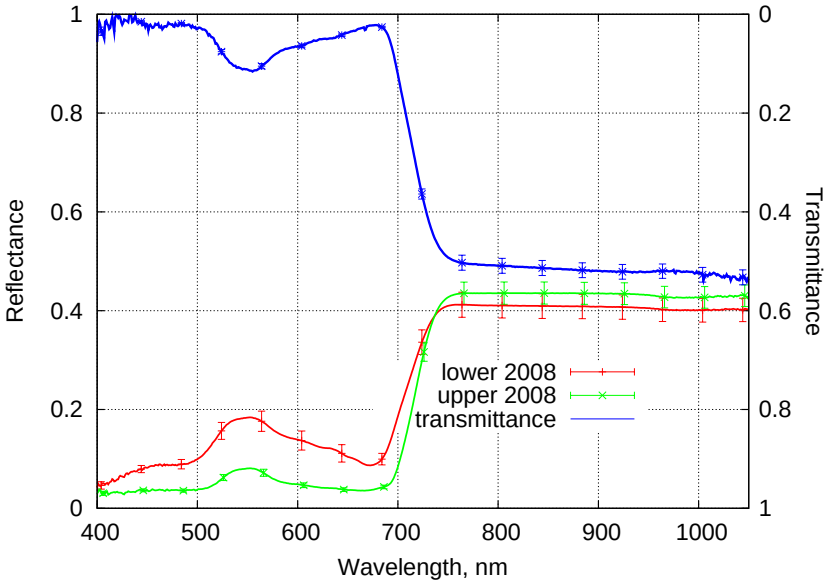

Figure 6.20: Leaf reflectance and transmittance of *Populus tremula*.

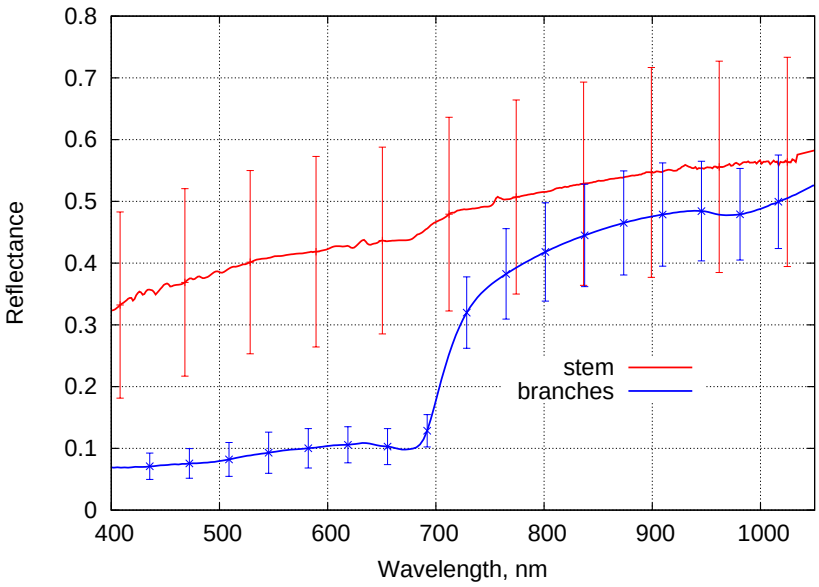

Figure 6.21: Stem and branch bark reflectance of *Betula pendula*. The stem bark was measured with GER-2600 in July 2001.

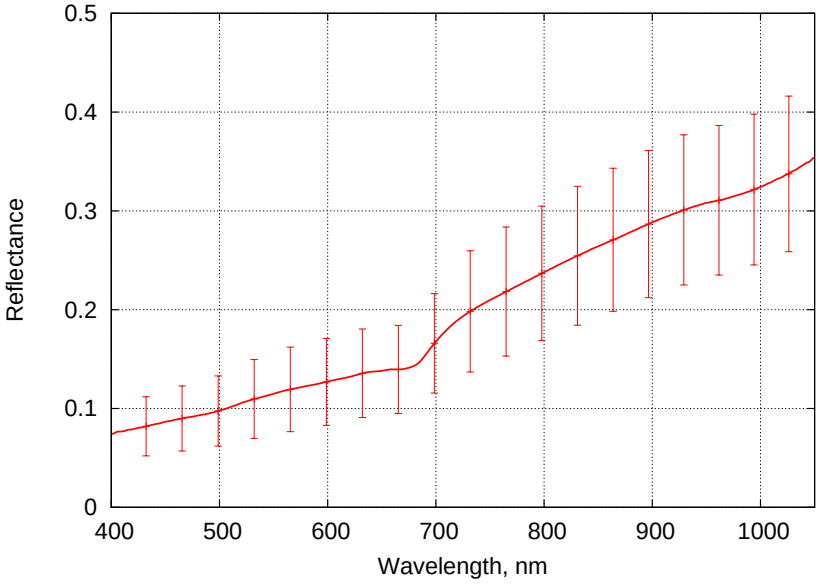

Figure 6.22: Stem bark reflectance of *Alnus glutinosa*.

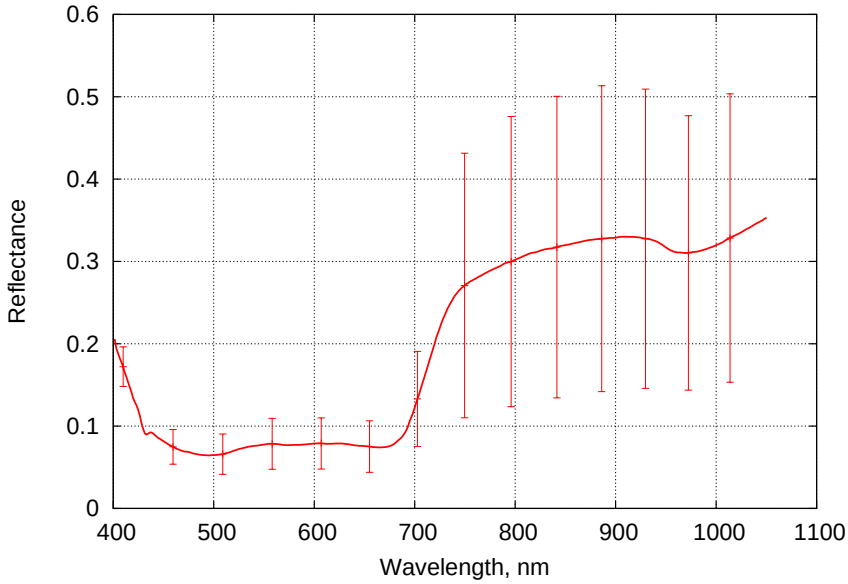

Figure 6.23: Stem bark reflectance of *Populus tremula*, BOREAS Old Aspen, August 1994 (Newcomer et al., 2000).

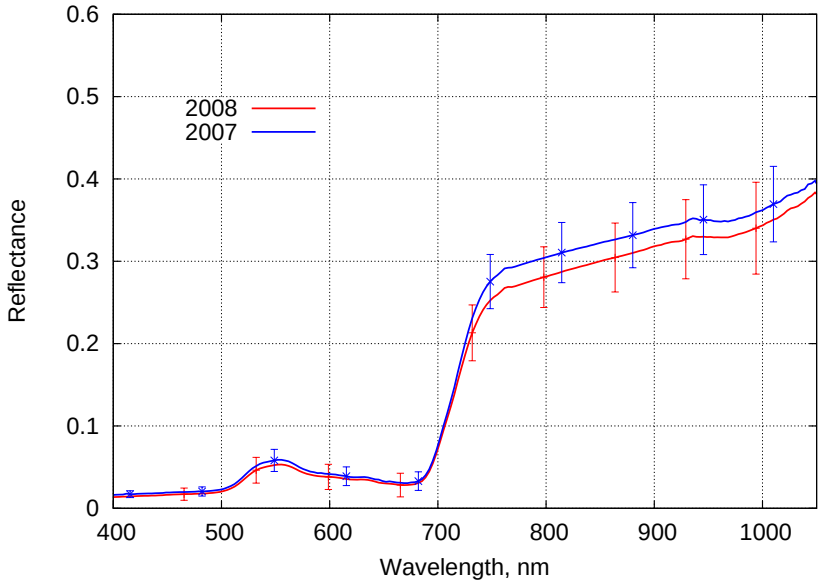

Figure 6.24: Average reflectance of understorey vegetation in the birch stand. Error bars show the standard deviation of nine mean reflectance at LAI points L1-L9.

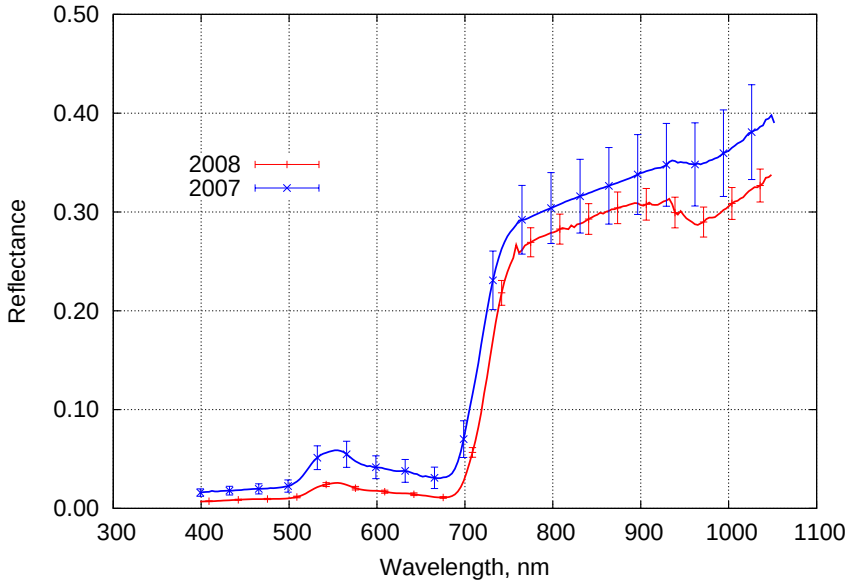

Figure 6.25: Average top-of-canopy nadir reflectance of the birch stand. Error bars show the standard error of the mean value.

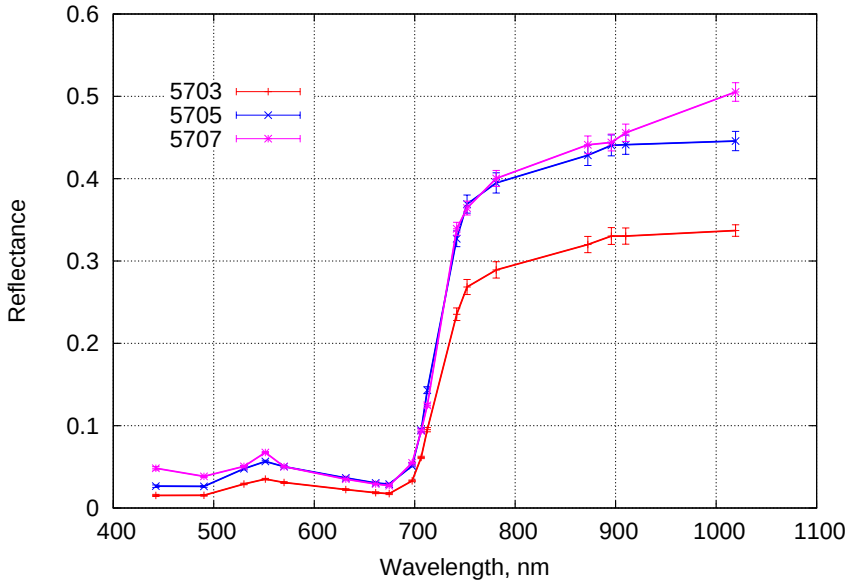

Figure 6.26: Average top-of-canopy directional reflectance of the birch stand from CHRIS images.

Figure 6.27: The birch stand in the CHRIS image: red - stand boundaries, yellow - the boundary of the study area, magenta - helicopter measurements in 2007, blue - helicopter measurements in 2008.

6.2.2 Pine stand

Structure

Pine (*Pinus sylvestris*) stand grows on the transitional bog. The soil is deep (>1.3 m) *Sphagnum* peat. The growth conditions are poor as indicated by H_{100} = 10.8 (stand height at age of 100 years) in the forest inventory database. Now the stand height is 15.6 meters, the stand is 124 years old, and stand density is 1122 trees per hectare. Forest understorey vegetation is composed of *Ledum palustre*, sparse *Eriophorum vaginatum*, and continuous *Sphagnum ssp.* moss layer.

Coordinates of the stand center are:
58° 18' 40.90" N 27° 17' 48.40" E
L-EST97: X:6468161.38 Y:693165.68.
The origin of local coordinates (x=0, y=0) is
L-EST97: X:6468117.13 Y:693110.54.
Azimuth of the y-coordinate is 6.25°.

The perspective and vertical view of the stand are in Figs 6.29 and 6.30, respectively.

Table 6.3: Mean tree parameters, the pine stand

Species	Code	N	H	$D_{1.3}$	L	R_{cr}
Upper layer						
Pinus sylvestris	MA	1115	15.9	18.0	4.2	1.5
Understorey						
Betula pendula	KS	6	4.1	5.5	2.9	0.8
Picea abies	KU	1	5.0	5.6	3.6	1.1

Notation see in Table 6.2

Figure 6.28: The pine stand, 10 May 2007.

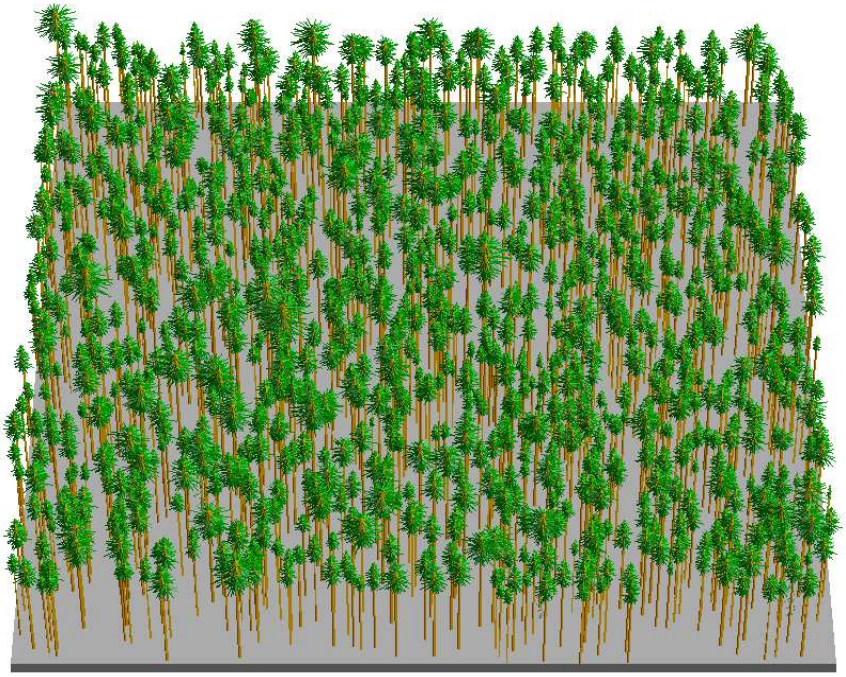

Figure 6.29: The pine stand, perspective view.

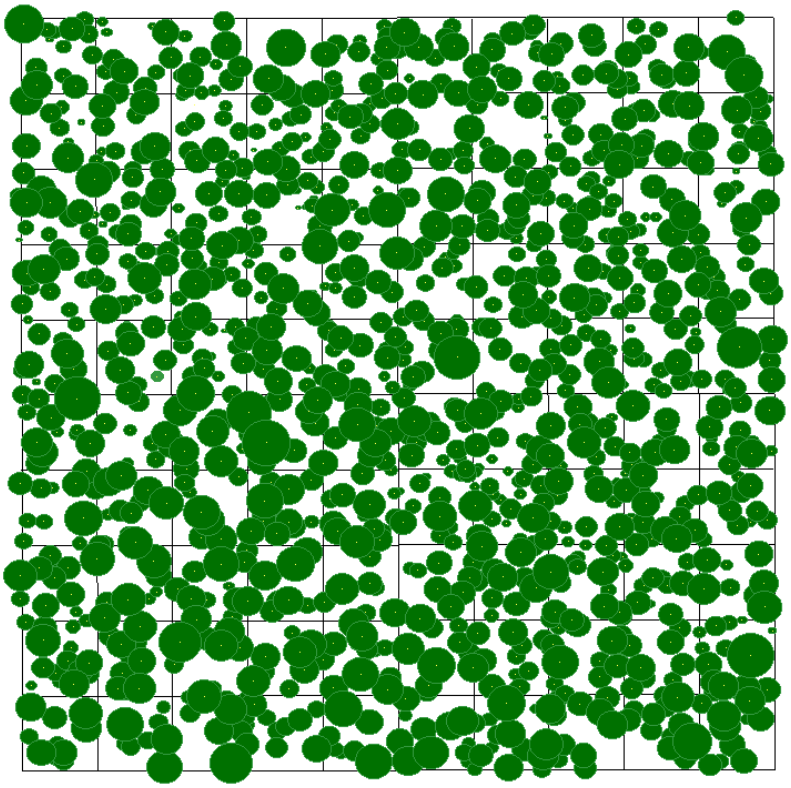

Figure 6.30: The pine stand, vertical view.

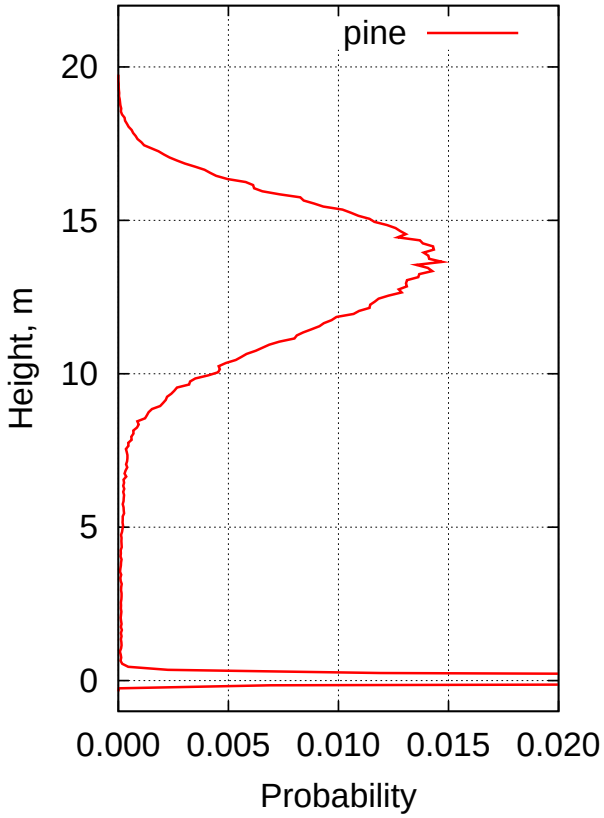

Figure 6.31: Vertical distribution of the lidar first return, the pine stand.

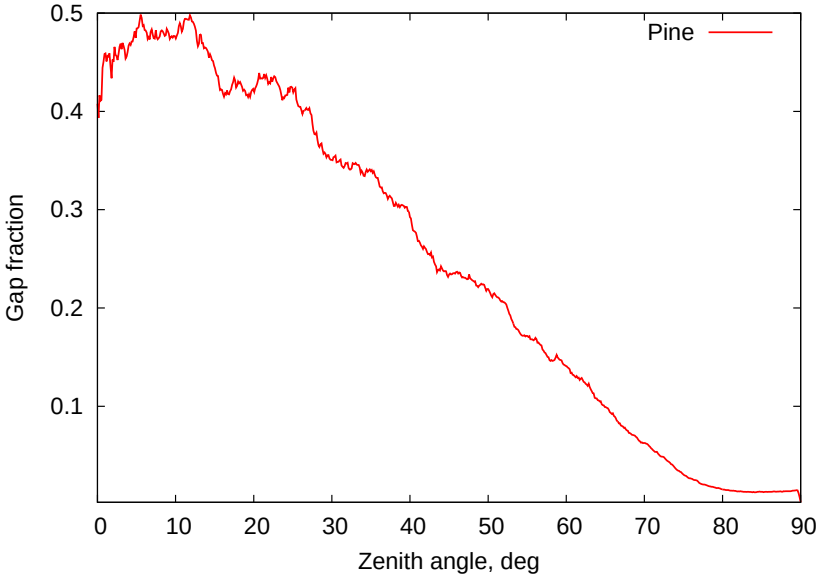

Figure 6.32: Gap fraction in the pine stand, 15.08.2008.

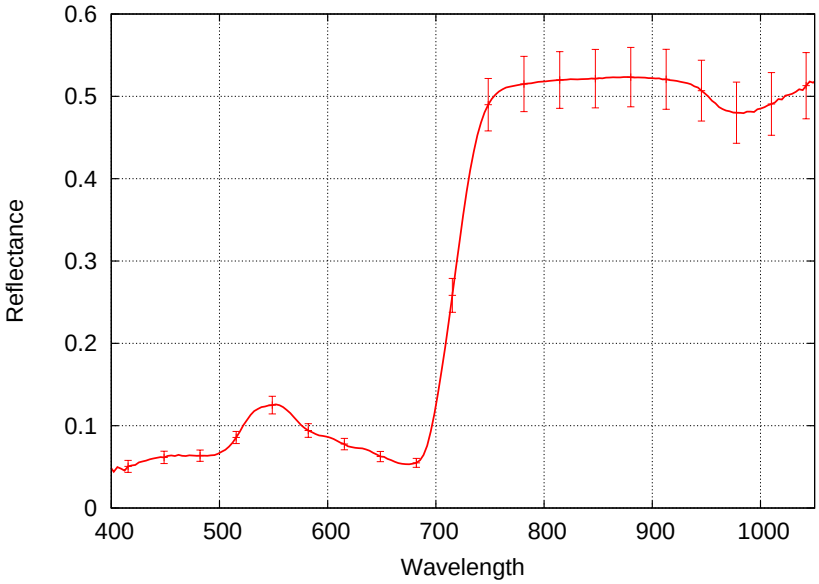

Figure 6.33: Reflectance of a bunch of needles of *Pinus silvestris*.

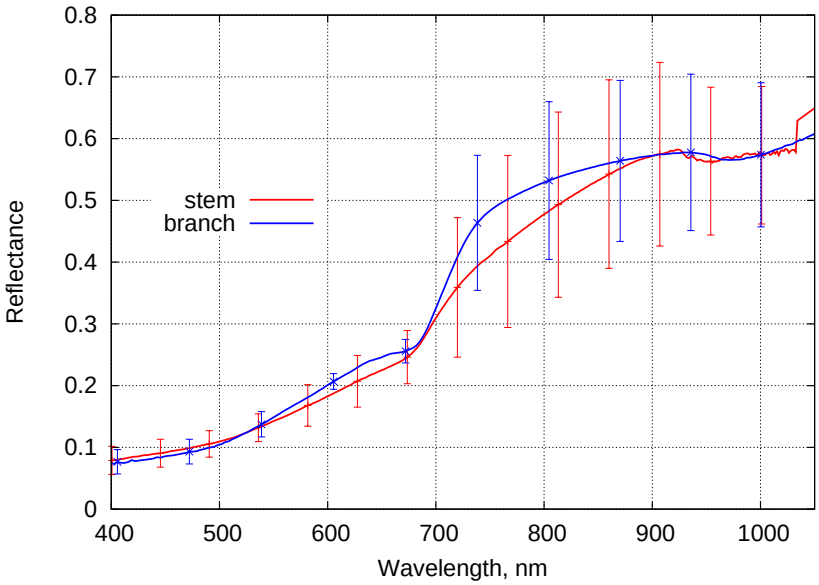

Figure 6.34: Reflectance of stem and branch bark of *Pinus silvestris*. The stem bark was measured with GER-2600 in July 2001.

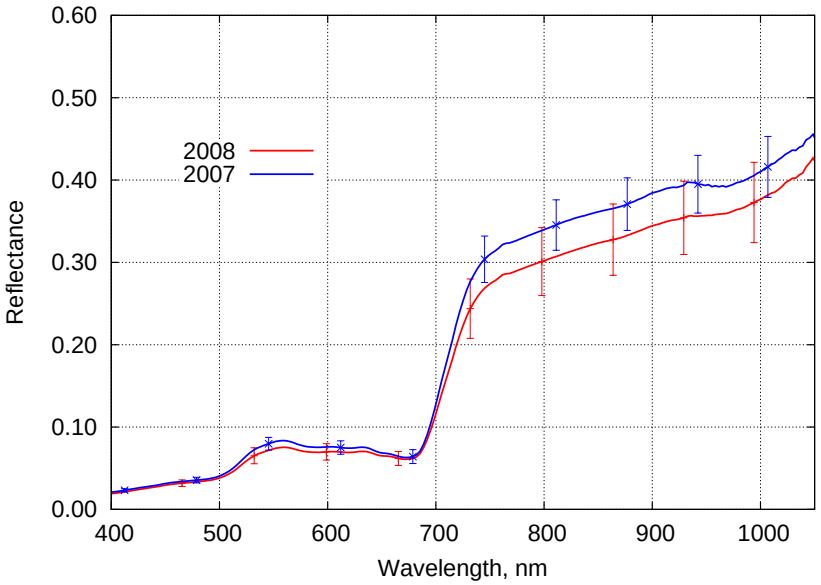

Figure 6.35: Average reflectance of understorey vegetation in the pine stand. Error bars show the standard deviation of nine mean reflectance at LAI points L1-L9.

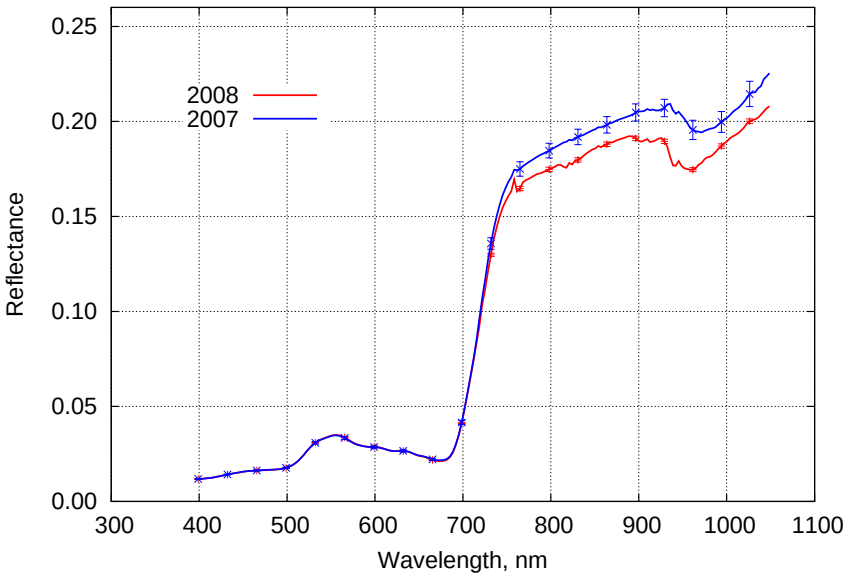

Figure 6.36: Average top-of-canopy nadir reflectance of the pine stand. Error bars show the standard error of the mean value.

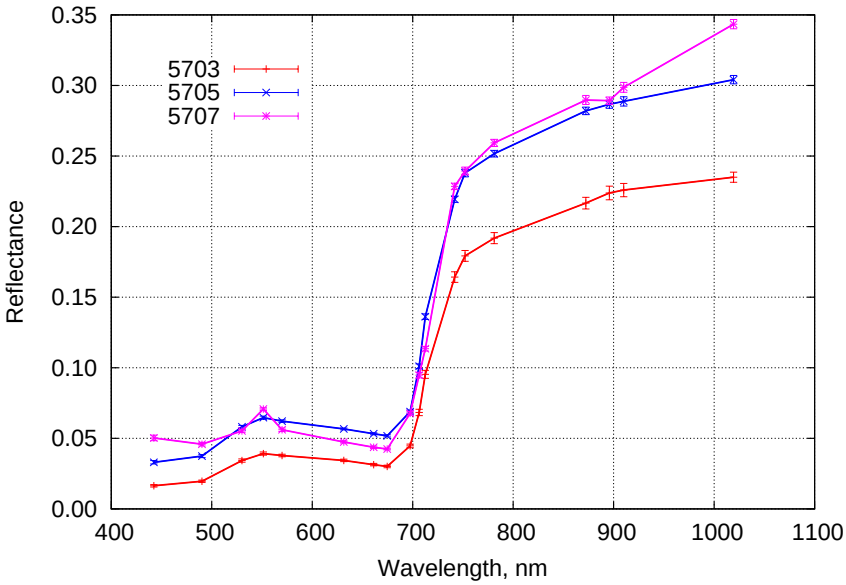

Figure 6.37: Average top-of-canopy directional reflectance of the pine stand from CHRIS images.

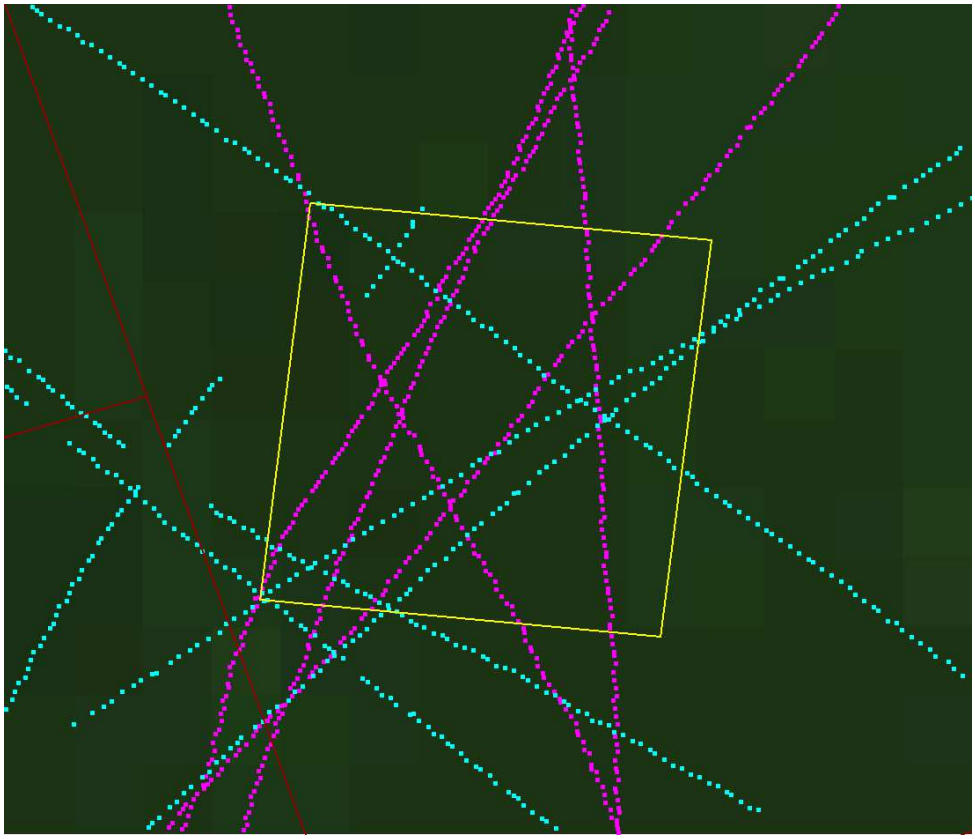

Figure 6.38: The pine stand in the CHRIS image: red - stand boundaries, yellow - the boundary of the study area, magenta - helicopter measurements in 2007, blue - helicopter measurements in 2008.

6.2.3 Spruce stand

Structure

Spruce (*Picea abies*) stand grows on a *Gleyi Ferric Podzol* site. However, the growth conditions are rather good (H_{100} = 29.1) because of drainage. Stand age is 59 years. There are two tree layers distinguishable according to the social status of the trees. Average height in the first (upper) layer is 23.2 meters and there are 774 trees per hectare. Stand density in the second (lower layer) is 915 trees per hectare and the height of trees ranges from 3.5 to 20 meters. Canopy cover is high (0.89) and, therefore, forest understorey vegetation is either partially missing or consists of mosses such as *Hylocomium splendens* or *Pleurozium schreberi*.

Coordinates of the stand center are:
58° 17' 43.0" N 27° 15' 22.0" E
L-EST97: X:6466255.8 Y:690873.1.
The origin of local coordinates (x=0, y=0) is
L-EST97: X:6466197.70 Y:690832.70.
Azimuth of the y-coordinate is 349.8°.

The perspective and vertical view of the stand are in Figs 6.40 and 6.41, respectively.

Table 6.4: Mean tree parameters, the spruce stand

Species	Code	N	H	$D_{1.3}$	L	R_{cr}
Upper layer						
Picea abies	KU	624	23.2	23.5	10.8	1.8
Betula pendula	KS	143	24.5	17.9	8.5	1.5
Alnus glutinosa	LM	3	22.4	20.3	9.6	2.1
Populus tremula	HB	2	25.1	18.3	6.9	1.5
Pinus sylvestris	MA	2	24.5	26.4	10.4	2.1
Second layer						
Betula pendula	KS	152	17.5	9.3	4.5	0.9
Picea abies	KU	517	13.8	11.1	6.3	1.2
Regeneration layer						
Picea abies	KU	157	8.0	6.9	4.4	1.1
Picea abies	KU	89	5.3	5.2	3.7	1.1

Notation see in Table 6.2

Figure 6.39: The spruce stand, 10 May 2007.

Optical properties

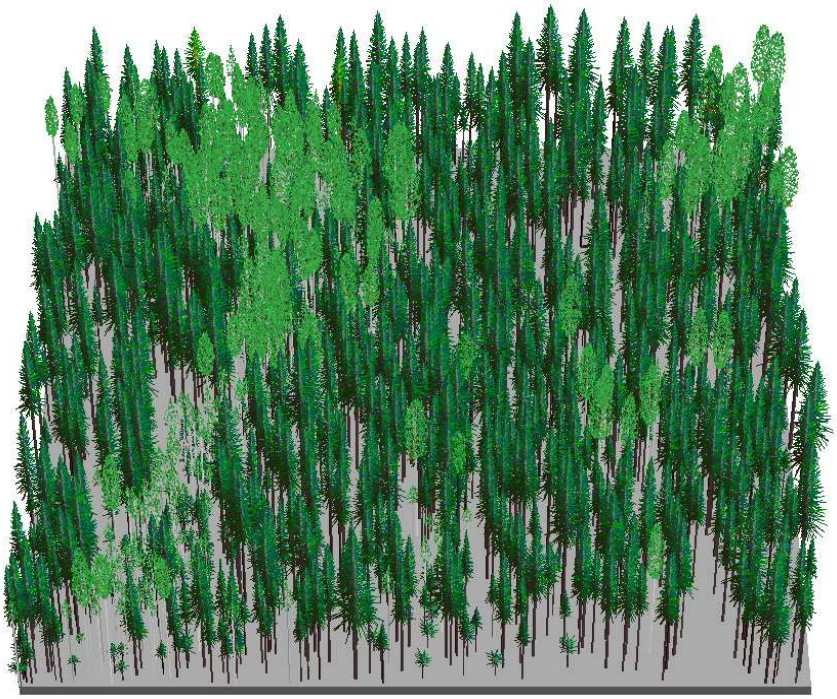

Figure 6.40: The spruce stand, perspective view.

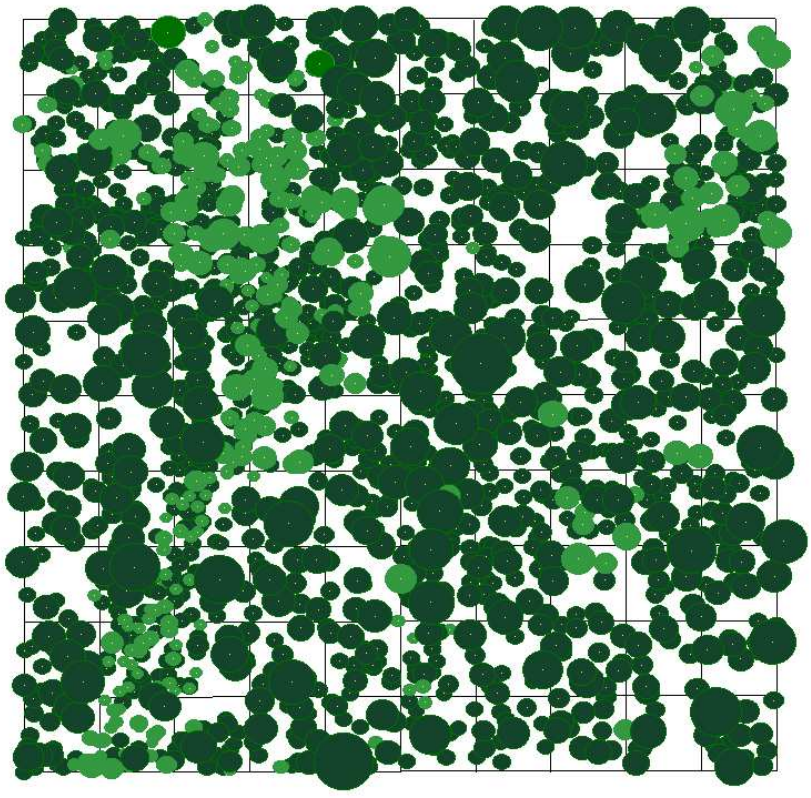

Figure 6.41: The spruce stand, vertical view.

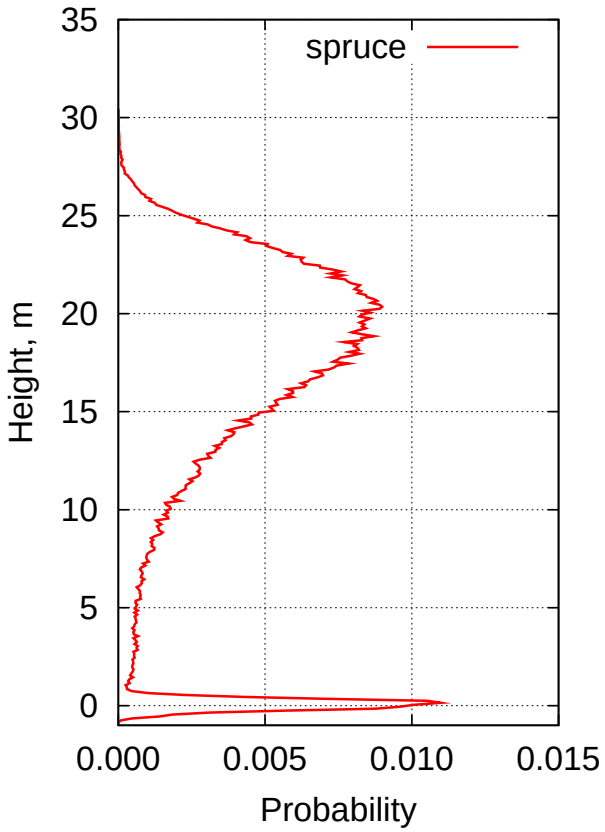

Figure 6.42: Vertical distribution of the lidar first return, the spruce stand.

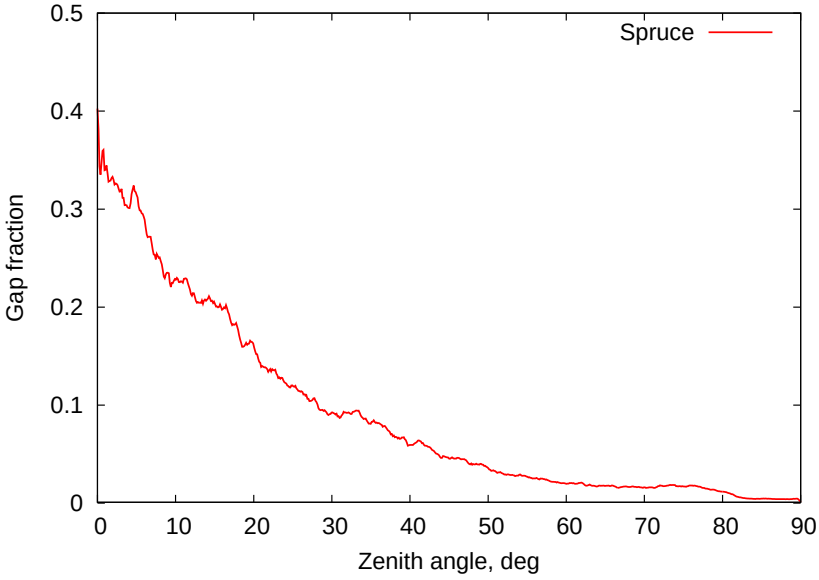

Figure 6.43: Gap fraction in the spruce stand, 15.08.2008.

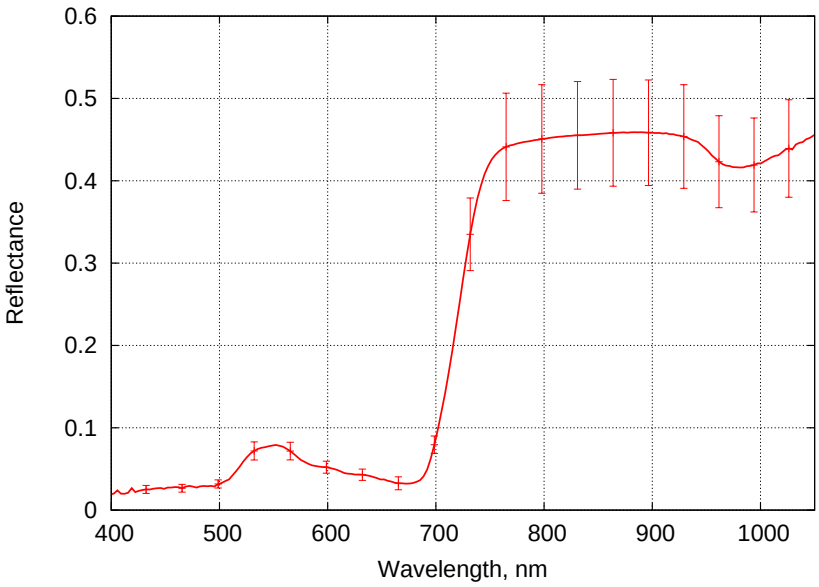

Figure 6.44: Reflectance of a bunch of needles of *Picea abies*.

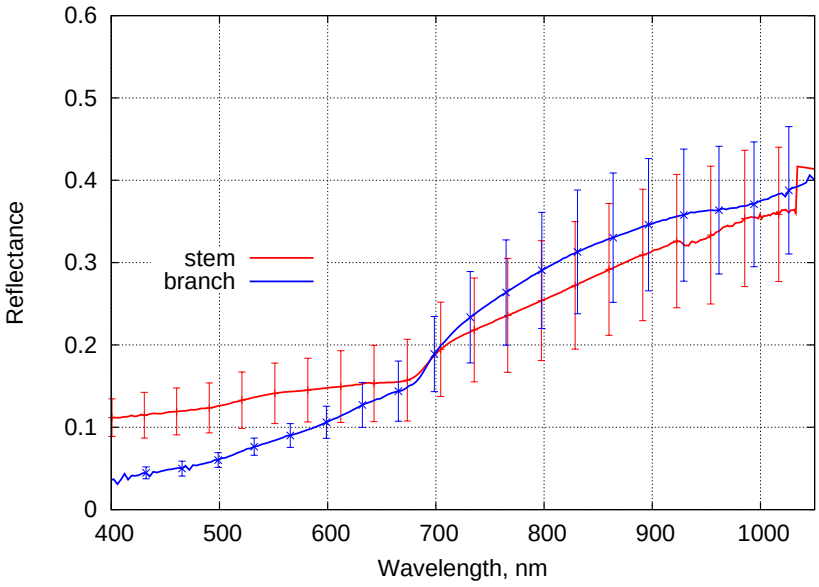

Figure 6.45: Reflectance of stem and branch bark of *Picea abies*. The stem bark was measured with GER-2600 in July 2001.

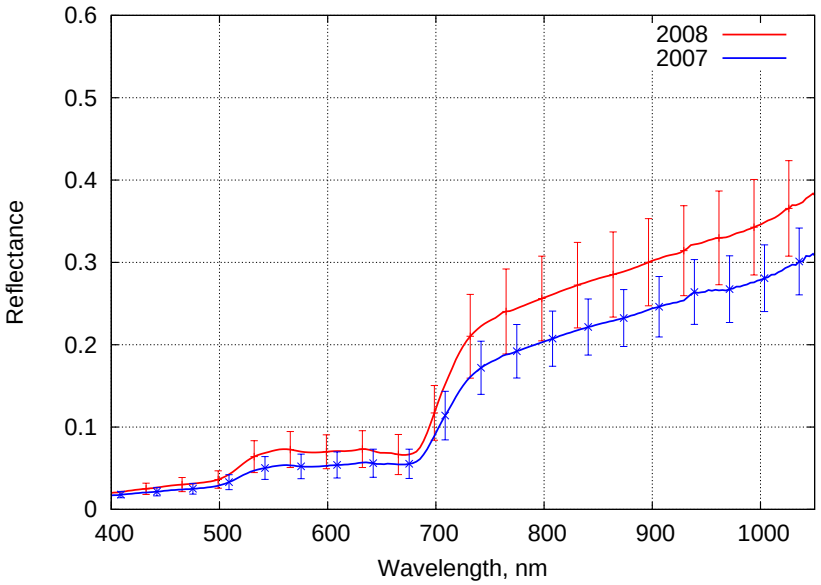

Figure 6.46: Average reflectance of understorey vegetation in the spruce stand. Error bars show the standard deviation of nine mean reflectance at LAI points L1-L9.

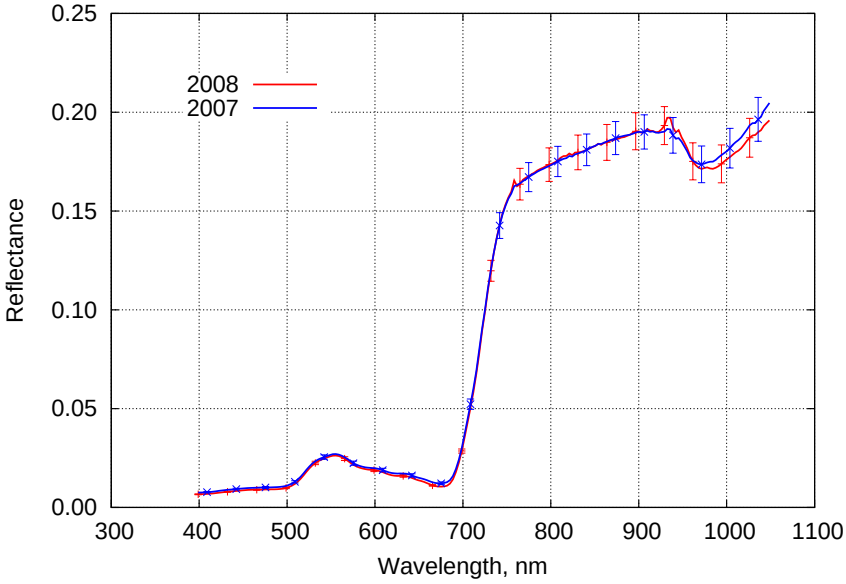

Figure 6.47: Average top-of-canopy nadir reflectance of the spruce stand. Error bars show the standard error of the mean value.

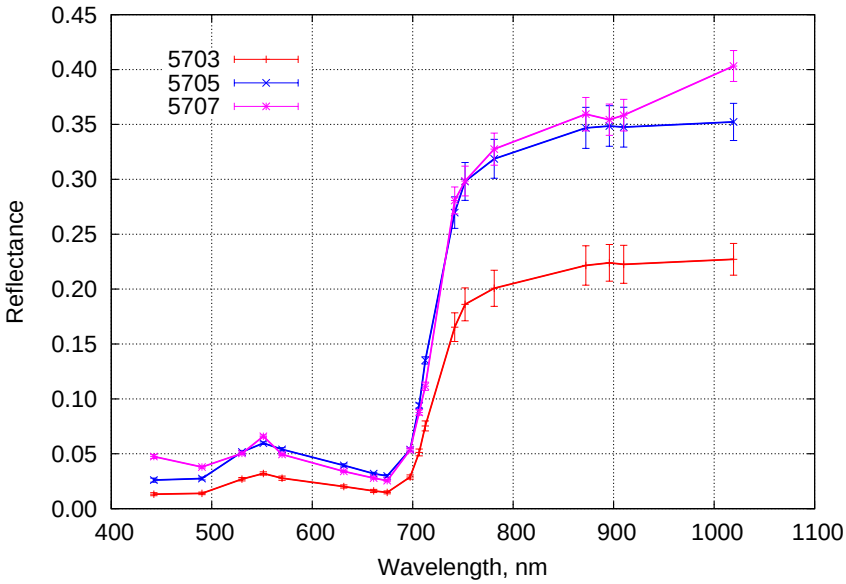

Figure 6.48: Average top-of-canopy directional reflectance of the spruce stand from CHRIS images.

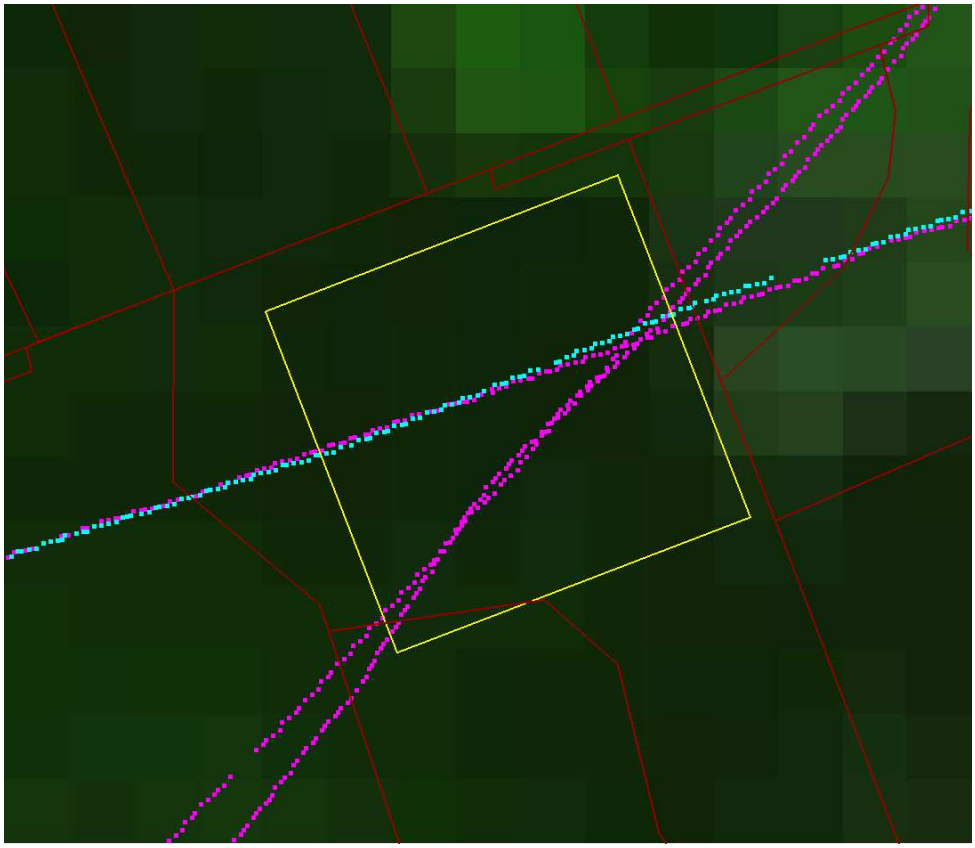

Figure 6.49: The spruce stand in the CHRIS image: red - stand boundaries, yellow - the boundary of the study area, magenta - helicopter measurements in 2007, blue - helicopter measurements in 2008.

Chapter 7

Discussion

Extensive ground based measurements of the structural and spectral properties have been performed at three forest stands near Järvselja, Estonia. This dataset is complemented by high resolution airborne measurements and multi-view hyperspectral CHRIS data.

The obtained tree location coordinates are in the radius of 5-20 cm of their true position. Standard errors of regression models for tree height, crown length and crown radius are 1.6 m, 1.7 m and 0.28 m, respectively. The compiled dataset of tree inventory parameters makes it possible to approximate individual crown architecture or calculate average estimates at stand or stand element level.

Low aerosol optical depth and water content of the atmosphere at so high geographical latitude, and good weather conditions during acquisition made atmospheric correction of satellite data less sensitive to atmosphere parameters. Top-of canopy helicopter measurements were used for the radiometric correction of CHRIS data. The radiometric quality of helicopter measurements is according to Eq. (5.11) determined by the gain and offset errors of spectrometers, and errors in the reference reflectance. The sensitivity of silicon-based sensors and gain coefficients do not change in the range of temperatures encountered. The applied stray light and aliasing correction removed artefacts in reflectance spectra and allow to extend the reliable spectral domain of the Zeiss MMS-1 spectrometer module. For the calibration we used a gray Spectralon panel which has certified reflectance spectrum with 0.5% variance. The footprint of the FOV of UAVSpec looking vertically on it was about 3 cm during calibration, therefore both the horizontal variance and deviation from Lambertian reflection of the reference panel may cause some systematic errors in the calibration of UAVSpec.

Helicopter measurements which were used for the vicarious calibration of CHRIS sensor were done one year later than CHRIS acquisition in the same phase of vegetation growth and in very similar illumination conditions. Several studies confirm that there is almost no change of reflectance of hemi-boreal mature stands in the age range of 40-60 years. Some changes of forest spectral reflectance in different years are possible, caused by changes in moisture conditions. The comparative study of forest hyperspectral reflectance at the test site in dry and normal summer revealed changes up to 10% in some wavelengths (Kuusk et al., 2008). As the summer 2006 of helicopter measurements was dry while in 2005 of CHRIS measurements we had normal amount of precipitation, the suggested correction factors may be systematically over-estimated in all spectral bands but red bands of chlorophyll absorption.

The impact of adjacency correction depends on the reflectance pattern of neighboring stands. The birch stand is surrounded by other broadleaved stands, thus the adjacency correction had almost no effect. As the wavelength dependence of pine stand reflectance differs from that of its neighbors, the relative impact varies with wavelength. There are recent clearcuts close to the spruce stand which have higher reflectance than the spruce stand throughout the whole VNIR spectrum, thus the adjacency correction decreased the stand reflectance 2-4%. In the whole CHRIS scene there are some stands which have significantly higher adjacency impact from targets of very contrasting reflectance (gravel roads, mowed grassland alongside of a dark stand). For some stands in some spectral bands the adjacency correction may reach even 15-20%.

CHRIS acquisition and helicopter measurements were at slightly different zenith angles. The leveling of the UAVSpec spectrometer during flight was controlled and adjusted using a bubble level. Systematic error in view direction was suppressed flying over test plots in forth and back directions. Swaying of the helicopter increases the effective field-of-view of the UAVSpec to some extent. The reflectance change due to different view angles was corrected by numerical simulations with the reflectance model FRT (Kuusk and Nilson, 2000). As stands of different structures have different angular dependence of directional reflectance (Rautiainen et al., 2004), some random error is added by this correction, the magnitude of which can be estimated only roughly.

Stem reflectance spectra measured with GER-2600 in (Lang et al., 2002) have no correction of spectral aliasing. The decrease of birch, pine and spruce stem reflectance between 920 and 1040 nm in Figs 6.21, 6.34 and 6.45 is partly an artefact caused by the spectral aliasing.

Both in helicopter measurements and in CHRIS images the signal variance due to noise is in most spectral bands significantly lower than the variance of target reflectance at so high spatial resolution. Thus the variance of reported spectra is mainly due the target variance and not the instrumental noise.

Chapter 8

Structure of the database

Data are organised in a directory tree. File formats and naming conventions are:

*.dat - tabulated data, ASCII,
*.txt - text files, ASCII,
*.plot - Gnuplot files for the visualization of data (ASCII),
*.png - x-y plots in PNG format (Portable Network Graphics),
*.jpg - hemispherical images in JPEG graphics format (Joint Photographic Experts Group),
*.tiff - thresholded hemispherical images in TIFF graphics format (Tag(ged) Image File Format),
jarvselja_db.pdf - the database description in the PDF Portable Document Format by Adobe Systems.

The list of files.

```
jarvselja2007
        |– birch
        |       |– chris
        |       |       |– 5703
        |       |       |       |– birch_5703.dat
        |       |       |       |– birch_chris.png
        |       |       |       |– birch_spec_5703.dat
        |       |       |       |– birch_spec_5703.plot
        |       |       |       ‘– birch_spec_5703.png
        |       |       |– 5705
        |       |       |       |– birch_spec_5705.dat
        |       |       |       |– birch_spec_5705.plot
        |       |       |       ‘– birch_spec_5705.png
        |       |       |– 5707
        |       |       |       |– birch_spec_5707.dat
        |       |       |       |– birch_spec_5707.plot
        |       |       |       ‘– birch_spec_5707.png
        |       |       |– chris_birch.dat
        |       |       |– chris_birch.plot
        |       |       ‘– chris_birch.png
        |       |– fisheye
        |       |       |– fe_22.11.2007
        |       |       |       |– L1.jpg
        |       |       |       |– L2.jpg
        |       |       |       |– L3.jpg
        |       |       |       |– L4.jpg
        |       |       |       |– L5.jpg
        |       |       |       |– L6.jpg
        |       |       |       |– L7.jpg
        |       |       |       |– L8.jpg
        |       |       |       |– L9.jpg
        |       |       |       ‘– readme.txt
        |       |       |– fe_29.07.2007
        |       |       |       |– L1.jpg
        |       |       |       |– L2.jpg
        |       |       |       |– L3.jpg
        |       |       |       |– L4.jpg
        |       |       |       |– L5.jpg
        |       |       |       |– L6.jpg
        |       |       |       |– L7.jpg
        |       |       |       |– L8.jpg
        |       |       |       ‘– L9.jpg
```

```
|       |       |– thresholded_22.11.2007
|       |       |       |– L1_t.tiff
|       |       |       |– L2_t.tiff
|       |       |       |– L3_t.tiff
|       |       |       |– L4_t.tiff
|       |       |       |– L5_t.tiff
|       |       |       |– L6_t.tiff
|       |       |       |– L7_t.tiff
|       |       |       |– L8_t.tiff
|       |       |       |– L9_t.tiff
|       |       |       ‘– readme.txt
|       |       ‘– thresholded_29.07.2007
|       |               |– L1_t.tiff
|       |               |– L2_t.tiff
|       |               |– L3_t.tiff
|       |               |– L4_t.tiff
|       |               |– L5_t.tiff
|       |               |– L6_t.tiff
|       |               |– L7_t.tiff
|       |               |– L8_t.tiff
|       |               |– L9_t.tiff
|       |               ‘– readme.txt
|       |– lai
|       |       |– cover_estimates_birch.txt
|       |       ‘– lai2000_birch.dat
|       |– leaves
|       |       |– leaves2007
|       |       |       |– rl_alder.dat
|       |       |       |– rl_alder.plot
|       |       |       |– rl_alder.png
|       |       |       |– rl_birch.dat
|       |       |       |– rl_birch.plot
|       |       |       |– rl_birch.png
|       |       |       |– rt_alder_lopex.dat
|       |       |       ‘– rt_birch_lopex.dat
|       |       ‘– leaves2008
|       |               |– rl_alder.dat
|       |               |– rl_alder.plot
|       |               |– rl_alder.png
|       |               |– rl_aspen.dat
|       |               |– rl_aspen.plot
|       |               |– rl_aspen.png
|       |               |– rl_birch.dat
|       |               |– rl_birch.plot
|       |               |– rl_birch.png
|       |               ‘– rl_birch_2.plot
|       |– readme.txt
|       |– stand_structure
|       |       |– birch_stand.dat
|       |       |– birch_stand.plot
|       |       |– birch_stand.png
|       |       |– p0_birch.dat
|       |       |– p0_birch.png
|       |       |– p0_birch_winter.dat
|       |       |– p0_birch_winter.png
|       |       ‘– lidar
|       |               |– birch_histz.png
|       |               |– histz.dat
|       |               ‘– histz.plot
|       |– stem
|       |       |– bark_alder.plot
|       |       |– bark_aspen.plot
|       |       |– bark_birch.plot
|       |       |– branch_birch.dat
|       |       |– branch_birch.png
|       |       |– stem_alder.dat
|       |       |– stem_alder.png
|       |       |– stem_aspen.dat
|       |       |– stem_birch.dat
|       |       ‘– stem_birch.png
|       |– uavspec
|       |       |– uavspec2007
|       |       |       |– birch_uav.dat
|       |       |       |– birch_uav.plot
|       |       |       ‘– birch_uav.png
|       |       ‘– uavspec2008
|       |               |– birch_uav.dat
|       |               |– birch_uav.plot
|       |               |– birch_uav.png
|       |               ‘– birch_uav2.plot
|       ‘– understorey
```

```
|                   |– photos
|                   |       |– *.jpg
|                   |– understorey2007
|                   |       |– birch_understorey.dat
|                   |       |– birch_understorey.plot
|                   |       `– birch_understorey.png
|                   `– understorey2008
|                           |– birch_understorey.dat
|                           |– birch_understorey.plot
|                           |– birch_understorey.png
|                           `– birch_understorey_2.plot
|– doc
|       `– jarvselja_db.pdf
|– pine
|       |– chris
|       |       |– 5703
|       |       |       |– pine_5703.dat
|       |       |       |– pine_chris.png
|       |       |       |– pine_spec_5703.dat
|       |       |       |– pine_spec_5703.plot
|       |       |       `– pine_spec_5703.png
|       |       |– 5705
|       |       |       |– pine_spec_5705.dat
|       |       |       |– pine_spec_5705.plot
|       |       |       `– pine_spec_5705.png
|       |       |– 5707
|       |       |       |– pine_spec_5707.dat
|       |       |       |– pine_spec_5707.plot
|       |       |       `– pine_spec_5707.png
|       |       |– chris_pine.dat
|       |       |– chris_pine.plot
|       |       `– chris_pine.png
|       |– fisheye
|       |       |– fe_29.07.2007
|       |       |       |– L1.jpg
|       |       |       |– L2.jpg
|       |       |       |– L3.jpg
|       |       |       |– L4.jpg
|       |       |       |– L5.jpg
|       |       |       |– L6.jpg
|       |       |       |– L7.jpg
|       |       |       |– L8.jpg
|       |       |       `– L9.jpg
|       |       `– thresholded_29.07.2007
|       |               |– L1_t.tiff
|       |               |– L2_t.tiff
|       |               |– L3_t.tiff
|       |               |– L4_t.tiff
|       |               |– L5_t.tiff
|       |               |– L6_t.tiff
|       |               |– L7_t.tiff
|       |               |– L8_t.tiff
|       |               |– L9_t.tiff
|       |               `– readme.txt
|       |– lai
|       |       |– cover_estimates_pine.txt
|       |       `– lai2000_pine.dat
|       |– needles
|       |       |– pine_needles.dat
|       |       |– pine_needles.plot
|       |       `– pine_needles.png
|       |– readme.txt
|       |– stand_structure
|       |       |– lidar
|       |       |       |– pine_histz.png
|       |       |       |– histz.dat
|       |       |       `– histz.plot
|       |       |– p0_pine.dat
|       |       |– p0_pine.png
|       |       |– pine_stand.dat
|       |       |– pine_stand.plot
|       |       `– pine_stand.png
|       |– stem
|       |       |– bark_pine.plot
|       |       |– bark_pine.png
|       |       |– branch_pine.dat
|       |       `– stem_pine.dat
|       |– uavspec
|       |       |– uavspec2007
|       |       |       |– pine_uav.dat
|       |       |       |– pine_uav.plot
```

```
|       |       |       `– pine_uav.png
|       |       `– uavspec2008
|       |               |– pine_uav.dat
|       |               |– pine_uav.plot
|       |               |– pine_uav.png
|       |               `– pine_uav2.plot
|       `– understorey
|               |– photos
|               |       |– *.jpg
|               |– understorey2007
|               |       |– pine_understorey.dat
|               |       |– pine_understorey.plot
|               |       `– pine_understorey.png
|               `– understorey2008
|                       |– pine_understorey.dat
|                       |– pine_understorey.plot
|                       |– pine_understorey.png
|                       `– pine_understorey2.plot
|– radiation
|       |– aeronet
|       |       |– almuc09082007.dat
|       |       |– almuc10072005.dat
|       |       |– almuc10072005.plot
|       |       |– almuc1020.plot
|       |       |– almuc24072008.dat
|       |       |– almuc26072006.dat
|       |       |– almuc440.plot
|       |       |– almuc675.plot
|       |       |– almuc870.plot
|       |       |– ppl09082007.dat
|       |       |– ppl10072005.dat
|       |       |– ppl1020.plot
|       |       |– ppl24072008.dat
|       |       |– ppl26072006.dat
|       |       |– ppl440.plot
|       |       |– ppl675.plot
|       |       `– ppl870.plot
|       |– fieldspec
|       |       |– 6s.dat
|       |       |– fs.dat
|       |       |– fs.plot
|       |       |– fs_08.08.2007.dat
|       |       |– fs_10.07.2005.dat
|       |       |– fs_24.07.2008.dat
|       |       `– fs_26.07.2006.dat
|       `– readme.txt
|– readme.txt
`– spruce
        |– chris
        |       |– 5703
        |       |       |– spruce_5703.dat
        |       |       |– spruce_chris.png
        |       |       |– spruce_spec_5703.dat
        |       |       |– spruce_spec_5703.plot
        |       |       `– spruce_spec_5703.png
        |       |– 5705
        |       |       |– spruce_spec_5705.dat
        |       |       |– spruce_spec_5705.plot
        |       |       `– spruce_spec_5705.png
        |       |– 5707
        |       |       |– spruce_spec_5707.dat
        |       |       |– spruce_spec_5707.plot
        |       |       `– spruce_spec_5707.png
        |       |– chris_spruce.dat
        |       |– chris_spruce.plot
        |       `– chris_spruce.png
        |– fisheye
        |       |– fe_22.07.2007
        |       |       |– L1.jpg
        |       |       |– L2.jpg
        |       |       |– L3.jpg
        |       |       |– L4.jpg
        |       |       |– L5.jpg
        |       |       |– L6.jpg
        |       |       |– L7.jpg
        |       |       |– L8.jpg
        |       |       `– L9.jpg
        |       `– thresholded_22.07.2007
        |               |– L1_t.tiff
        |               |– L2_t.tiff
        |               |– L3_t.tiff
```

```
|                   |– L4_t.tiff
|                   |– L5_t.tiff
|                   |– L6_t.tiff
|                   |– L7_t.tiff
|                   |– L8_t.tiff
|                   |– L9_t.tiff
|                   `– readme.txt
|– lai
|       |– cover_estimates_spruce.txt
|       `– lai2000_spruce.dat
|– needles
|       |– spruce_needles.dat
|       |– spruce_needles.plot
|       `– spruce_needles.png
|– readme.txt
|– stand_structure
|       |– lidar
|       |       |– spruce_histz.png
|       |       |– histz.dat
|       |       `– histz.plot
|       |– p0_spruce.dat
|       |– p0_spruce.png
|       |– spruce_stand.dat
|       |– spruce_stand.plot
|       `– spruce_stand.png
|– stem
|       |– bark_spruce.plot
|       |– bark_spruce.png
|       |– branch_spruce.dat
|       `– stem_spruce.dat
|– uavspec
|       |– uavspec2007
|       |       |– spruce_uav.dat
|       |       |– spruce_uav.plot
|       |       `– spruce_uav.png
|       `– uavspec2008
|               |– spruce_uav.dat
|               |– spruce_uav.plot
|               |– spruce_uav.png
|               `– spruce_uav2.plot
`– understorey
        |– photos
        |       |– *.jpg
        |– understorey2007
        |       |– spruce_understorey.dat
        |       |– spruce_understorey.plot
        |       `– spruce_understorey.png
        `– understorey2008
                |– spruce_understorey.dat
                |– spruce_understorey.plot
                |– spruce_understorey.png
                `– spruce_understorey2.plot
```

8.1 Data access

Järvselja data are available from the Tartu Observatory as compressed tar-archive files:
jarvselja_db.tar.gz - the complete database,
jarvselja_birch.tar.gz, jarvselja_pine.tar.gz, jarvselja_spruce.tar.gz - subsets of the database.

Contact:
andres@to.ee (Andres Kuusk).

8.2 Acknowledgments

When data are used from this data set, the collection should be cited as:

Kuusk, A., Lang, M., Kuusk, J., Lükk, T., Nilson, T., Mõttus, M., Rautiainen, M., and Eenmäe, A. Database of optical and structural data for the validation of radiative transfer models. Technical report, Ver. 04.2015. Tartu Observatory.

Instead, the following publications could be referred to:
Kuusk, A., Lang, M., and Kuusk, J. (2013). Database of optical and structural data for the validation of forest radiative transfer models. In: Alexander A. Kokhanovsky (Editor), Radiative Transfer and Optical Properties of Atmosphere and Underlying Surface. Light Scattering Reviews 7. Springer, 109-148.

Kuusk, A., Kuusk, J., and Lang, M. (2009) A dataset for the validation of reflectance models. Remote Sensing of Environment, 113(5), 889-892, doi:10.1016/j.rse.2009.01.005.

The image data presented in this report have been provided by the European Space Agency, using the ESA PROBA platform and the Surrey Satellite Technology Ltd CHRIS instrument. The Sun-photometer data are provided by the International AERONET Federation, we thank Drs. O. Kärner and M. Sulev for their effort in establishing and maintaining the Tõravere AERONET site. The work of M. Rautiainen was supported by the Academy of Finland (COOLFUTURE project). The European Commission's DG Joint Research Center (Ispra, Italy) supported the collection of field data. The study has been funded by Estonian target financed projects SF0062466s03 and SF0060115s08, and by Estonian Science Foundation, Grants no. 6100, 6812 and 6815.

Contacts

andres@to.ee (Andres Kuusk)
lang@to.ee (Mait Lang)
joel@to.ee (Joel Kuusk)
tonu.lukk@neti.ee (Tõnu Lükk)
matti.mottus@helsinki.fi (Matti Mõttus)
nilson@to.ee (Tiit Nilson)
miina.rautiainen@helsinki.fi (Miina Rautiainen)
alo.eenmae@metsad.ee (Alo Eenmäe)

Bibliography

Abdou, W. A., Bruegge, C. J., Helmlinger, M. C., Conel, J. E., Pilorz, S. H., Ledeboer, W., Gaitley, B. J., and Thome, K. J. (2002). Vicarious calibration experiment in support of the Multi-angle Imaging SpectroRadiometer. *IEEE Transactions on Geoscience and Remote Sensing*, 40 (7), 1500–1511.

Banham, M.R. and Katsaggelos, A.K. (1997). Digital image restoration. *IEEE Signal Processing Magazine,* 14(2), 24-41.

Barnsley, M.J., Settle, J.J., Cutter, M.A., Lobb, D.R., and Teston, F. (2004). The PROBA/CHRIS mission: A low-cost smallsat for hyperspectral multiangle observations of the earth surface and atmosphere. *IEEE Transactions on Geoscience and Remote Sensing,* 42(7), 1512-1520.

Begiebing, S. and Bach, H., 2004. Analyses of hyperspectral and directional CHRIS data for agricultural monitoring using a canopy reflectance model. Proc. of the 2nd CHRIS/Proba Workshop, ESA/ESRIN, Frascati, Italy 28-30 April (ESA SP-578, July 2004).

Cannizzaro, J.P. and Carder, K.L. (2006). Estimating chlorophyll a concentrations from remote-sensing reflectance in optically shallow waters. *Remote Sensing of Environment,* 101(1), 13-24.

CHRIS (2002): The CHRIS Instrument. http://www.chris-proba.org.uk/frames/index2.html

Cutter, M. (2004). Review of aspects associated with the CHRIS calibration. In: Proc. of the 2nd ESA CHRIS/Proba Workshop, 28-30 April, ESRIN, Frascati, Italy. No. SP-578. ESA, pp. 1–5, CD-ROM.

Cutter, M. and Johns, L., 2005. CHRIS data products - latest issue. Proc. of the 3rd ESA CHRIS/Proba Workshop, 21¿23 March, ESRIN, Frascati, Italy, (ESA SP-593, June 2005), 6 pp.

Deschamps, P.Y., Breon, F.M., Leroy, M., Podaire, A., Bricaud, A., Buriez, J.C., and Seze, G. (1994). The POLDER mission - instrument characteristics and scientific objectives. *IEEE Transactions on Geoscience and Remote Sensing* 32(3), 598-615.

Elterman, L. (1968). *UV, Visible, and IR Attenuation for Altitudes to 50 km. Rep. AFCRL-68-0153*, U.S. Air Force Cambridge Research Laboratory, Bedford, Mass.

ESRI (2007). ESRI world basemap data. Web page http://www.esri.com/data/download/basemap/index.html (accessed 01.10.2007).

Feng, H., Campbell, J.W., Dowell, M.D., and Moore, T.S., 2005. Modeling spectral reflectance of optically complex waters using bio-optical measurements from Tokyo Bay. Remote Sensing of Environment, 99(3), 232-243.

Froidefond, J.M., Gardel, L., Guiral, D., Parra, M., and Ternon, J.F. (2002). Spectral remote sensing reflectances of coastal waters in French Guiana under the Amazon influence. *Remote Sensing of Environment,* 80(2), 225-232.

Guanter, L., Alonso, L., and Moreno, J., 2005. A method for the surface reflectance retrieval from PROBA/CHRIS data over land: Application to ESA SPARC campaigns. IEEE Transactions on Geoscience and Remote Sensing, 43(12), 2908-2917.

Hadjimitsis, D.G., Clayton, C.R.I., and Hope, V.S. (2004). An assessment of the effectiveness of atmospheric correction algorithms through the remote sensing of some reservoirs. *International Journal of Remote Sensing,* 25(18), 3651-3674.

Hoffmann, C.W. and Usoltsev, V.A. (2002). Tree-crown biomass estimation in the forest species of the Ural and of Kazakhstan. *Forest Ecology and Management*, 158, 59-69.

Holben, B.N., Eck, T.F., Slutsker, I., Tanre, D., Buis, J.P., Setzer, A., Vermote, E., Reagan, J.A., Kaufman, Y.J., Nakajima, T., Lavenu, F., Jankowiak, I., and Smirnov, A. (1998). AERONET - A federated instrument network and data archive for aerosol characterization. *Remote Sensing of Environment,* 66(1), 1-16.

HYSPLIT (2007): HYbrid Single-Particle Lagrangian Integrated Trajectory Model Version 4.8. http://www.arl.noaa.gov/ready/hysp_info.html.

Jennings, S.B., Brown, N.D., and Sheil, D. (1999). Assessing forest canopies and understorey illumination: canopy closure, canopy cover and other measures. *Forestry,* 72(1), 59-74.

Johansson, T. (1999), Dry matter amount and increment in 21- to 91-year-old common alder and gray alder and some practical implications. *Canadian Journal of Forest Research*, *29*(11), 1679–1690.

Johansson, T. (2000). Biomass equations for determining fractions of common and gray alders growing on abandoned farmland and some practical implications. *Biomass and Bioenergy*, 18, 147-159.

Järvselja (2007). Järvselja Experimental and Training Forest District. Web page http://www.jarvselja.ee/

Korhonen, L., Korhonen, T.K., Rautiainen, M., Stenberg, P. (2006). Estimation of forest canopy cover: a comparison of field measurement techniques. *Silva Fennica,* 40(4), 577-588.

Kostkowski, H.J., 1997. *Reliable spectroradiometry* (La Plata, Md.: Spectroradiometry Consulting).

Kuusk A. (1994). A multispectral canopy reflectance model. *Remote Sensing of Environment,* 50(2), 75-82.

Kuusk A. (1998). Monitoring of vegetation parameters on large areas by the inversion of a canopy reflectance model. *International Journal of Remote Sensing,* 19(15), 2893-2905.

Kuusk, A., Kuusk, J., and Lang, M. (2009). A dataset for the validation of reflectance models. *Remote Sensing of Environment,* 113(5), 889-892.

Kuusk, A., Kuusk, J., and Lang, M. (2014). Measured spectral bidirectional reflection properties of three mature hemiboreal forests. *Agricultural and Forest Meteorology,* 185, 14-19.

Kuusk, A., Lang, M., and Kuusk, J. (2013). Database of optical and structural data for the validation of forest radiative transfer models. In: Alexander A. Kokhanovsky (Editor), *Radiative Transfer and Optical Properties of Atmosphere and Underlying Surface. Light Scattering Reviews 7.* Springer, 109-148.

Kuusk, J., Kuusk, A., Lang, M., and Lükk, T. (2008). Satellite-measured forest hyperspectral reflectance for the validation of reflectance models. *International Journal of Applied Earth Observation and Geoinformation*, submitted.

Kuusk, A., Nilson, T., 2000. A directional multispectral forest reflectance model. Remote Sensing of Environment, 72, 244-252.

Lang, M., Jürjo, M., Adermann, V., and Korjus, H. (2006). Integrated approach for quantitative assessment of illegal forest fellings in Estonia. *Baltic Forestry,* 12(1), 103 - 109.

Liang, S.L., Fang, H.L., and Chen, M.Z. (2001). Atmospheric correction of Landsat ETM+ land surface imagery - Part I: Methods. *IEEE Transactions on Geoscience and Remote Sensing,* 39(11), 2490-2498.

Liang, S. (2004). *Quantitative Remote Sensing of Land Surfaces*, Hoboken, New Jersey: Wiley-Interscience, 534 pp.

Lang, M., Kuusk, A., Nilson, T., Lükk, T., Pehk, M., and Alm, G. (2002). Reflectance spectra of ground vegetation in sub-boreal forests. Web page http://www.aai.ee/bgf/ger2600/

Marklund, L.G. (1988). *Biomass functions for pine, spruce and birch in Sweden.* Tech. Rep., Vol. 45. (pp. 73). Umeå, Sweden Swedish University of Agricultural Sciences, Department of Forest Survey.

Martin, J. G., B. D. Kloeppel, T. L. Schaefer, D. L. Kimbler, and S. G. McNulty (1998). Aboveground biomass and nitrogen allocation of ten deciduous southern Appalachian tree species. *Canadian Journal of Forest Research*, *28*, 1648–1659.

McGaughey, R. J. (1997). Visualizing forest stand dynamics by using the stand visualization system. In: *Proceedings ACSM/ASPRS Annual convention and Exposition Seattle, WA. Betsheda*, Vol. 4, pp. 248–257, MD: American Society for Photogrammetry and Remote Sensing.

McPeters, R. (2007). Total Ozone Mapping Spectrometer. http://jwocky.gsfc.nasa.gov/

McRoberts, R.E. and Tomppo, E.O. (2007). Remote sensing support for national forest inventories. *Remote Sensing of Environment,* 110, 412-419.

MODIS Amosphere Terra Images. http://modis-atmos.gsfc.nasa.gov/IMAGES/

Newcomer, J., Landis, D., Conrad, S., Curd, S., Huemmrich, K., Knapp, D., Morrell, A., Nickeson, J., Papagno, A., Rinker, D., Strub, R., Twine, T., Hall, F., Sellers, P., Eds., 2000. Collected Data of The Boreal Ecosystem-Atmosphere Study. NASA. CD-ROM.

Niinemets, Ü., Kull, K. (1994). Leaf weight per area and leaf size of 85 Estonian woody species in relation to shade tolerance and light availability. *Forest Ecology and Management,* 70, 1-10.

Nilson, T. and Kuusk, A.(2004). Improved algorithm for estimating canopy indices from gap fraction data in forest canopies. *Agricultural and Forest Meteorology,* 124(3-4), 157-169.

Novo, E.M.L.M., Pereira, W., and Melack, J.M. (2004). Assessing the utility of spectral band operators to reduce the influence of total suspended solids on the relationship between chlorophyll concentration and the bidirectional reflectance factor in Amazon waters. *International Journal of Remote Sensing,* 25(22), 5105-5116.

Podilchuk, C. (1998). Signal recovery from partial information. In: Madisetti, V.K., Williams, D.B. (Eds.), *The Digital Signal Processing Handbook*, (pp. 25-1–25-21). Boca Raton: CRC Press LLC.

Pensa, M., and A. Sellin (2002). Needle longevity of Scots pine in relation to foliar nitrogen content, specific leaf area, and shoot growth in different forest types. *Canadian Journal of Forest Research*, *32*(7), 1225–1231.

R-project (2007), The R Project for Statistical Computing, web-page http://www.r-project.org/.

Rabiner, L.R. and Gold, B. (1975). *Theory and Application of Digital Signal Processing.* Engelwood Cliffs: Prentice-Hall.

Rautiainen, M., Stenberg, P., Nilson, T., and Kuusk, A. (2004). The effect of crown shape on the reflectance of coniferous stands. *Remote Sensing of Environment*, 89(1), 41–52.

Reinersman, P.N. and Carder, K.L. (1995) Monte Carlo simulation of the atmospheric point-spread function with an application to correction for the adjacency effect. *Applied Optics*, 34(21), 4453–4471.

Schaepman, M. and Dangel, S., 2000. Solid laboratory calibration of a nonimaging spectroradiometer. *Applied Optics*, 39, 3754–3764.

Sellin, A. (2000). Estimating the needle area from geometric measurements: Application of different calculation methods to Norway spruce. *Trees*, 14(4), 215-222, 819.

Slater, P.N., Biggar, S.F., Thome, K.J., Gellman, D.I., and Spyak, P.R. (1996). Vicarious radiometric calibrations of EOS sensors. *Journal of Atmospheric and Oceanic Technology*, 13(2), 349–359.

Slater, P.N. and Biggar, S.F. (1996). Suggestions for radiometric calibration coefficient generation. *Journal of Atmospheric and Oceanic Technology* 13(2), 376–382.

Song, C. and Woodcock, C.E. (2003). Monitoring forest succession with multitemporal Landsat images: Factors of uncertainty. *IEEE Transactions on Geoscience and Remote Sensing,* 41(11), 2557-2567.

Tamm, Ü. (2000). *Aspen in Estonia.* Eesti Loodusfoto, Tartu, pp 125-134.

Thome, K., Markham, B., Barker, J., Slater, P., and Biggar, S., 1997. Radiometric calibration of Landsat. Photogrammetric Engineering & Remote Sensing, 63(7):853-858.

VALERI (2005): http://www.avignon.inra.fr/valeri/, accessed on March 15, 2005.

Vermote, E.F., Tanre, D., Deuze, J.L., Herman, M., and Morcrette, J.J. (1997). Second simulation of the satellite signal in the solar spectrum, 6S - An overview. *IEEE Transactions on Geoscience and Remote Sensing,* 35(3), 675-686.

Wang, C. (2006), Biomass allometric equations for 10 co-occurring tree species in Chinese temperate forests. *Forest Ecology and Management*, *222*, 9–V16.

Wendlandt, W.W. and Hecht, H.G. (1966). *Reflectance Spectroscopy*, Wiley, 298 pp.

Widlowski, J.-L., Verstraete, M.M., Pinty, B., and Gobron, N. (2003). Allometric relationships of selected European tree species. Tech. rep., EC Joint Research Centre, Ispra, Italy.

Widlowski, J.-L., Taberner, M., Pinty, B., Bruniquel-Pinel, V., Disney, M., Fernandes, R., Gastellu-Etchegorry, J.-P., Gobron, N., Kuusk, A., Lavergne, T., Leblanc, S., Lewis, P.E., Martin, E., Mõttus, M., North, P.R.J., Qin, W., Robustelli, M., Rochdi, N., Ruiloba, R., Soler, C., Thompson, R., Verhoef, W., Verstraete, M.M., and Xie, D. (2007). Third radiation transfer model intercomparison (RAMI) exercise: Documenting progress in canopy reflectance models. *Journal of Geophysical Research,* 112(D09111), doi:10.1029/2006JD007821.

Document revision history

Changes	Date	Version
Added new sets of hemispherical photos: 05 August 2013 15 August 2013 (Spruce) 22 April 2015 (Pine)	30 April 2015	Ver. 04.2015
Updated the coordinates of the study plot in the pine stand	15 Sept 2014	Ver. 09.2014
Added gap fraction angular profiles from hemispherical photos	20 March 2012	Ver. 03.2012
Added lidar scanner data: Instrument and measurement description Vertical distribution of lidar first return Updated the corner coordinates of stands	30 Sept 2009	Ver. 09.2009
Revised CHRIS calibration data Replaced Fig. 5.3 Added doi of Remote Sens. Environ. paper Added Document revision history	25 Feb 2009	Ver. 02.2009
Base document created	11 Nov 2008	Ver. 11.11.2008